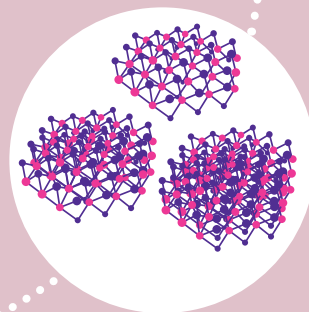
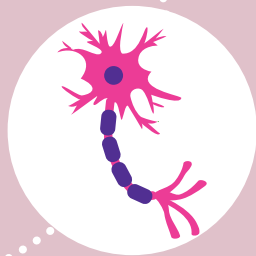
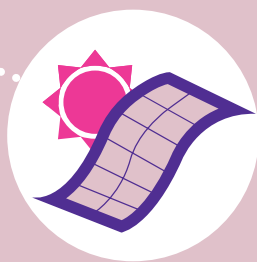


Material Matters™

VOLUME 15 • NUMBER 1



Disruptive Materials

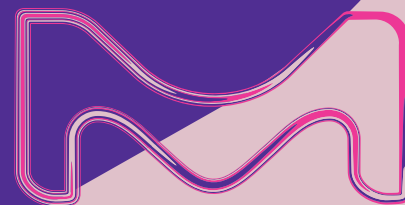
Organic and Optoelectronics

MXenes: A Tunable Family of 2D Carbides and Nitrides with Diverse Applications

Synthesis and Applications of Graphene Nanoribbons Synthesized via Top-Down Methods

Recent Technology Advancements in the Fabrication of Integrated Organic Electronics

Recent Progress for High Performance Tandem Organic Solar Cells



The life science business of Merck KGaA, Darmstadt, Germany operates as MilliporeSigma in the U.S. and Canada.

Introduction



Na Li, Ph.D.
Product Manager -
Electronic Materials

Welcome to the first issue of *Material Matters*™ for 2020, focusing on disruptive research advancements enabled by materials innovation. This issue highlights a few recent breakthroughs associated with new material discoveries related to nanomaterials, organic solar cells, and organic thin film transistors.

In our first article, **Professor Gogotsi** and **Dr. Shuck** (Drexel University, USA) introduce MXenes: a rising family of two-dimensional materials with a unique combination of high conductivity, hydrophilicity, and extensive tunability and how they are impacting a broad range of research fields, from enabling ultrahigh-capacity energy devices, tunable optical devices, and high-performance electronics, to the facilitation of new theranostics.

Solar energy is the ultimate source of clean energy. One of the biggest challenges lies in how to most effectively harvest and store solar energy as electricity. In our second article, **Professor Chen** (Nankai University, China) and his team explain the strategies behind their recent record-breaking organic solar cells, reaching a power conversion efficiency of 17.3%. They review the development of new non-fullerene acceptors, their computer-guided material selection method, and the tandem cell design.

Transistors are the fundamental building blocks of electronic circuits. Recently, the development of advanced organic semiconductors has inspired new innovations for a variety of organic integrated circuits. In our third article, **Professor Tokito** and **Professor Takeda** (Yamagata University, Japan) share their new materials, device architecture design principles, and performance optimization protocols for printed and solution-processed, low-cost, highly flexible, organic electronic devices.

Graphene nanoribbons, a classic type of carbon nanomaterials, possessing both carbon nanotube-like high aspect-ratio and graphene-like high surface-area, have already been used in multiple applications. In our final article, **Professor Tour** (Rice University, USA) and his colleagues explore new insights in the top-down fabrication of graphene nanoribbons with controlled edge functionalization and intact basal planes. These insights are leading to exciting new applications such as spinal cord regeneration, dendrite-free lithium ion batteries, and spray-on superhydrophobic anti-icing coatings.

Each article in this publication is accompanied by a list of relevant Sigma-Aldrich materials available from MilliporeSigma. For additional product information, visit us at [SigmaAldrich.com/matsci](https://www.sigmaaldrich.com/matsci). Please bother us with your new product suggestions, as well as thoughts and comments for *Material Matters*™ at [SigmaAldrich.com/technicalservice](https://www.sigmaaldrich.com/technicalservice).

About the Cover

Materials innovation is one of the greatest driving forces behind technological revolution. Many of the biggest challenges we face today await solutions based on promising materials and innovative materials applications. In this issue, the cover art illustrates a few recent examples where disruptive materials have provided significant contributions towards solutions for some of our most pressing challenges in clean energy, health, and the environment.

Merck KGaA, Darmstadt, Germany
Frankfurter Strasse 250
64293 Darmstadt, Germany
Phone +49 6151 72 0

To Place Orders / Customer Service

Contact your local office or visit
[SigmaAldrich.com/order](https://www.sigmaaldrich.com/order)

Technical Service

Contact your local office or visit
[SigmaAldrich.com/techinfo](https://www.sigmaaldrich.com/techinfo)

General Correspondence

Contact your local office or visit
[SigmaAldrich.com/techinfo](https://www.sigmaaldrich.com/techinfo)

Subscriptions

Request your FREE subscription to *Material Matters*™ at [SigmaAldrich.com/mm](https://www.sigmaaldrich.com/mm)

The entire *Material Matters*™ archive is available at [SigmaAldrich.com/mm](https://www.sigmaaldrich.com/mm)

Material Matters™ (ISSN 1933-9631) is a publication of Merck KGaA, Darmstadt, Germany

Copyright © 2020 Merck KGaA, Darmstadt, Germany and/or its affiliates. All rights reserved. MilliporeSigma, the vibrant M, Sigma-Aldrich and Material Matters are trademarks of Merck KGaA, Darmstadt, Germany or its affiliates. All other trademarks are the property of their respective owners. Detailed information on trademarks is available via publicly accessible resources. More information on our branded products and services on [MilliporeSigma.com](https://www.milliporesigma.com)

Your Material Matters



Bryce P. Nelson, Ph.D.
Materials Science Initiative Lead

Dr. Rafael Furlan de Oliveira of Institut de Science et d'Ingénierie Supramoléculaires (Université de Strasbourg, France) recommended the addition of a series of prefabricated OFET device components and measuring tools. These products have been introduced to our catalog to aid in the fabrication of organic electronic devices and evaluation: back-gated OFET interdigitated substrates (**FIPMS148**, **FIPMS223**, **FIPMS175**), back-gated LOFET circuit substrates (**FIPMS267**), back-gated OFET substrates (no gold) (**FIPMS176**), and OFET Miniprober (**FIPMS990**). These prefabricated OFET substrates are produced in a clean room on silicon wafers with thermal silicon dioxide as full-area dielectrics, and patterned gold electrodes via lift-off technology to ensure high device reliability and reproducibility. The back-gated OFET interdigitated substrates enable fabrication of several devices, with different electrode dimensions and high channel width-to-length ratios (500–4000) on a single chip through the deposition of the semiconductor layer only.¹⁻³ The back-gated LOFET circuit substrates provide further simplified material characterization through the analysis of basic logic circuits and avoid time-consuming analysis of individual transistors. OFET Miniprobers allows fast and easy device measurement without the need of a probe station, samplers or manipulator pins, while enabling reliable pad contact to these prefabricated OFET substrates.

References

- (1) Schmode, P.; Savva, A.; Kahl, R.; Ohayon, D.; Meichsner, F.; Dolynchuk, O.; Thurn-Albrecht, T.; Inal, S.; Thelakkat, M. *ACS Appl. Mater. Interfaces* **2020**, *12* (11), 13029–13039.
- (2) Paternò, G. M.; Robbiano, V.; Fraser, K. J.; Frost C.; Sakai G.; Cacialli F. *Sci Rep* **2017**, *7*, 41013.
- (3) Mirka, B.; Fong, D.; Rice, N. A.; Melville, O. A.; Adronov, A.; Lessard, B. H. *Chem. Mater.* **2019**, *31* (8), 2863–2872.

Name	Description	Cat. No.
Back-gated OFET Interdigitated Substrate	16 transistors per chip Au source/drain, 230 nm SiO ₂ gate-insulator varied W/L from 500 to 4000	FIPMS148-1PAK
	16 transistors per chip Au source/drain, 230 nm SiO ₂ gate-insulator varied W/L from 500 to 4000	FIPMS175-1PAK
Back-gated OFET Substrate	n-doped silicon wafer with 230 nm SiO ₂ gate-insulator	FIPMS176-1PAK
Back-gated OFET Interdigitated Substrate	16 transistors per chip Au source/drain, 90 nm SiO ₂ gate-insulator varied W/L from 500 to 4000	FIPMS223-1PAK
Back-gated LOFET Circuit Substrate	200 nm gate-insulator Au contact Ti/TiN source/drain inverters and ring oscillators transistors	FIPMS267-1PAK
OFET Miniprober	Measuring Adaptor for Back-Gated OFET Interdigitated Substrates	FIPMS990-1EA

Table of Contents

Articles

MXenes: A Tunable Family of 2D Carbides and Nitrides with Diverse Applications	3
Synthesis and Applications of Graphene Nanoribbons Synthesized via Top-Down Methods	11
Recent Technology Advancements in the Fabrication of Integrated Organic Electronics	21
Recent Progress for High Performance Tandem Organic Solar Cells	33

Featured Products

MXene Precursor-MAX Phases A list of MXene materials	8
Etchants A selection of etchants for MXene processing	8
Graphene and Graphite Selections of graphene and graphite materials	9
2D Nanomaterial Inks and Powders A selection of BNNT, graphene, and MoS ₂ inks	9
Materials for Bioelectronic A selection of NIR emitters and graphene QD materials	17
Graphene-Based Materials A list of devices, 3D printing inks, composites, GO, and nanoribbons	17
Carbon Nanomaterials A list of carbon nanotube inks and carbon nanotubes	18
Organic Thin-Film Transistor Materials A selection of N-type and P-type semiconductors	28
Prefabricated Device Components for Organic Field-Effect Transistors A list of OFET device components	28
Conductive Inks for Printed Electronics A selection of screen, inkjet, flexographic, LIFT, 3D, and gravure printing inks	29
Dielectric Inks for Printed Electronics A selection of inkjet and screen printing inks	30
Interfacial Inks for Printed Electronics A selection of slot die, doctor blade, and spin coating inks	30
Non-Fullerene Acceptors A list of non-fullerene acceptors	38
Polymeric Donors A list of wide-, medium-, and low-bandgap polymeric donors	42
Interfacial Materials A selection of hole-transport and other buffer layer materials	45
Building Blocks A selection of building blocks	47
Electronic Materials A selections of electronic grade electrolytes, substrates, and electrode materials	48

From MAX Phase to MXene

MXene is a promising new family of 2D nanomaterials, consisting of conductive 2D carbides, nitrides, and carbonitrides.

First described by Professor Yury Gogotsi from Drexel University in 2011, MXenes combine both metallic conductivity and hydrophilic nature, due to their hydroxyl or oxygen terminated surfaces functional groups. They typically can be synthesized via top-down selective etching of their layered precursor materials, MAX phases.

MXene offers:

- High solution processability
- High conductivity
- High surface area
- High electrochemical activity

MXene are widely reported in applications such as:

- Conductive electronic devices
- Energy storage devices
- Sensors and biosensors
- Multifunctional composites
- Water purification
- Catalyst

[SigmaAldrich.com/mxene](https://www.sigmaaldrich.com/mxene)



© 2020 Merck KGaA, Darmstadt, Germany and/or its affiliates. All Rights Reserved. MilliporeSigma, the vibrant M and Sigma-Aldrich are trademarks of Merck KGaA, Darmstadt, Germany or its affiliates. All other trademarks are the property of their respective owners. Detailed information on trademarks is available via publicly accessible resources.

30386 01/2020

The life science business of Merck KGaA, Darmstadt, Germany operates as MilliporeSigma in the U.S. and Canada.

Sigma-Aldrich®
Lab & Production Materials

MXenes: A Tunable Family of 2D Carbides and Nitrides with Diverse Applications



Christopher E. Shuck and Yury Gogotsi*

A. J. Drexel Nanomaterials Institute and Department of Materials Science and Engineering, Drexel University, Philadelphia, PA 19104, USA
*Email: gogotsi@drexel.edu

Introduction

Two-dimensional (2D) materials have been the focus of significant research due to their unique electronic, optical, and mechanical properties. Since the discovery of the unusual physical properties of graphene in 2004, research groups around the world have focused on the discovery, development, and applications of 2D materials. Following the development of graphene, a wide variety of other 2D families have been explored, including recently discovered single elemental structures (phosphorene (Cat. No. **902896**), stanene, silicene, germanene (Cat. No. **906026**), etc.), and known binary compounds (BN (Cat. Nos. **901349**, **901410**), transition metal dichalcogenides (TMDs) (Cat. Nos. **901867**, **901187**, **902462**, **903841**), oxides, etc.), or more complex compositions, such as clays. In 2011, a family of conductive 2D carbides, nitrides, and carbonitrides, known as MXenes, was discovered.¹

MXenes are potentially the largest class of 2D materials known today, with more than 30 different types reported (Figure 1), and hundreds computationally studied *in-silico*. Moreover, there exists the potential for thousands of additional members of this family if solid solutions are included.² MXenes have the general structure $M_{n+1}X_nT_x$, where M is an early transition element (Ti, V, Nb, etc.) and X is C and/or N, with n ranging from 1–4.³ T_x represents the surface terminations (typically -O, -OH, and -F), with $n+1$ layers of M covering n layers of X in the arrangement of $[MX]_nM$. These conductive, hydrophilic 2D ceramics are synthesized via top-down selective etching of their precursor materials MAX phases (Cat. Nos. **910740**, **910767**, **910775**, **910759**, **910821**, **910708**), typically in the form of $M_{n+1}AX_n$, but some MXenes are synthesized from different precursors, including M_2A_2X and $M_{n+1}A_xX_{n+x}$ as well. The synthesis of MXenes

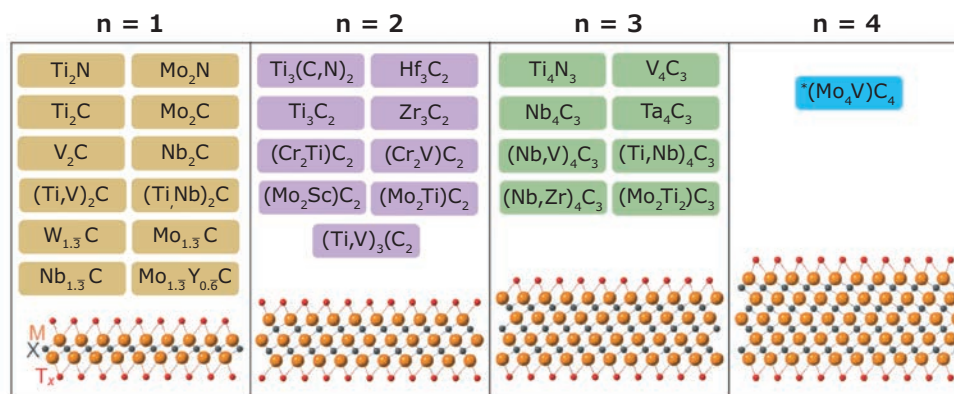


Figure 1. MXene compositions reported to date. MXenes have the general structure $M_{n+1}X_nT_x$ where M is an early transition metal (Ti, V, Nb, etc.), X is C and/or N, T_x are the surface terminations (typically -O, -OH, -Cl and -F), and $n = 1-4$. MXenes discovered to date include mono-M MXenes, ordered double-transition metal MXenes, solid-solution MXenes, and ordered divacancy MXenes. Adapted from reference 3.

has been shown to be readily scalable, with no change in the properties as the batch size is increased.⁴ In these cases, A is primarily Al, but Si and Ga have also been used.² MXenes come in multiple forms: single metal element structures ($\text{Ti}_3\text{C}_2\text{T}_x$, Ti_2CT_x , V_2CT_x , etc.), ordered double transition metal MXenes (i.e., $\text{Mo}_2\text{Ti}_2\text{C}_3\text{T}_x$, $\text{Mo}_2\text{TiC}_2\text{T}_x$, $\text{Cr}_2\text{TiC}_2\text{T}_x$, etc.), solid-solution MXenes (i.e., $\text{Ti}_{2-y}\text{V}_y\text{CT}_x$, $\text{Mo}_{4-y}\text{V}_y\text{C}_3\text{T}_x$, $\text{Ti}_{2-y}\text{Nb}_y\text{CT}_x$), and ordered divacancy MXenes ($\text{Mo}_{1.33}\text{CT}_x$, $\text{W}_{1.33}\text{CT}_x$, etc.).² The MXene family is quite diverse, with the materials that can be tuned through a variety of approaches, including modification of the number of atomic layers (n), changing the M or X elements, adjusting the surface chemistry (T_x) through post-treatment or during synthesis, size selection of MXenes, and intercalation of different species into the structure, among multiple other approaches.²

MXenes typically come in two forms, multilayer (ML) powder or delaminated single flakes. To synthesize ML MXene powder, typically fluoride-containing etchants (HF or HF/HCl) are used to selectively remove the A (in most cases Al) layer. To convert the ML powder into a single-flake colloidal solution, an intercalant (i.e., LiCl, tetramethylammonium hydroxide (TMAOH), dimethyl sulfoxide (DMSO), etc.) is used.⁵ Another approach where the precursor is simultaneously etched and delaminated using an *in-situ* HF formation approach (HCl+LiF, NH_4HF_2 (Cat. No. 455830), etc.) can be used.⁵ Because MXenes are primarily synthesized via a topochemical process in an aqueous environment, they maintain a hydrophilic nature. Due to this hydrophilicity, MXenes can be processed using standard solution-based techniques (primarily water-based), including vacuum filtration, spray-coating, dip-coating, spin-coating, etc. In addition to aqueous solvents, MXenes form stable colloidal solutions in polar organic solvents, including dimethylformamide (DMF), *N*-methyl-2-pyrrolidone (NMP), propylene carbonate (PC), and ethanol.⁶ Due to their extensive customizability (e.g., composition, surface terminations, thickness, etc.) and processability, MXenes have already found use in multiple diverse fields, including energy storage devices, biomedical applications, composite materials, electrochromic devices, and countless other applications (Figure 2).

Applications of MXenes

The first application of MXenes was as energy storage materials. $\text{Ti}_3\text{C}_2\text{T}_x$, for example, was shown to have a volumetric capacitance of up to $1,500 \text{ F cm}^{-3}$.⁸ Considering this property, it is expected that thinner (M_2XT_x) MXenes can have a higher theoretical gravimetric capacity. Significant work has focused on utilization of various MXenes as energy storage materials.⁹ Within energy storage devices, MXenes have been used as electrodes in electrochemical capacitors, micro-supercapacitors, and batteries, utilizing Li-, Na-, Mg-, Al-, and other chemistries, with a wide variety of electrolytes being used, including aqueous (e.g., H_2SO_4 , Li_2SO_4 , KOH, etc.) and non-aqueous organic (e.g., DMSO, PC, acetonitrile (ACN), etc.)-based solutions (Figure 3),

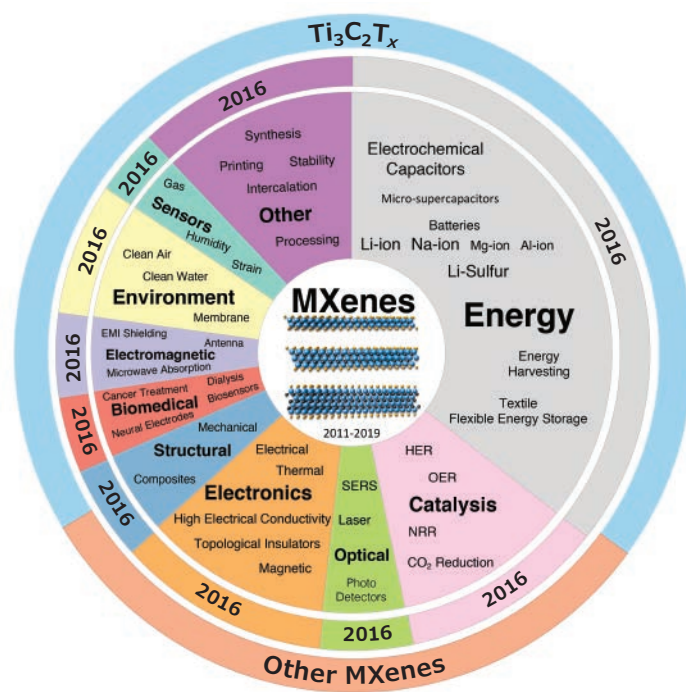


Figure 2. Applications and properties of MXenes explored to date. The center pie chart shows the ratio of publications in each application/property of MXenes with respect to the total number of publications on the “MXene” topic from 2011 to February 2019 based on *Web of Science*. The middle pie chart ring, with similar color to the center one, shows the starting year for exploration of each application/property of MXenes. There might be one or two papers published before some of the mentioned years; we considered a year with a few important publications as the starting year for each slice. The outer ring shows the ratio of publications *only* on $\text{Ti}_3\text{C}_2\text{T}_x$ MXene versus the publications on all MXene compositions (M_2XT_x , $\text{M}_2\text{X}_2\text{T}_x$, $\text{M}_2\text{X}_3\text{T}_x$, and $\text{M}_5\text{X}_4\text{T}_x^*$). Adapted with permission from 2, copyright 2019 Springer and 7, copyright 2019 American Chemical Society.

in addition to ionic liquids.^{2, 9-11} Depending on the electrolyte system used, the usable voltage range can extend from 0.5 to 3.0 V.² Due to the large number of inherent chemistries available to MXenes, significant work has been done to examine the charge storage mechanisms of various MXenes, as well as how to further optimize the materials. MXenes typically have a pseudocapacitive storage mechanism; the ions penetrate between MXene sheets, interacting with the surface terminations on the basal plane. Depending on the ions used, the MXene interlayer spacing can be varied, accommodating the size of the intercalating ion.¹² Finally, MXenes have excellent cyclability, with no change in the capacitance recorded after 10,000 cycles for $\text{Ti}_3\text{C}_2\text{T}_x$ in aqueous electrolytes.¹¹ The use of metallic-conductive MXenes as binders and current collectors in energy storage devices is also very promising. While a significant portion of MXene research has focused on energy storage capabilities, a wide variety of other applications have also been explored.

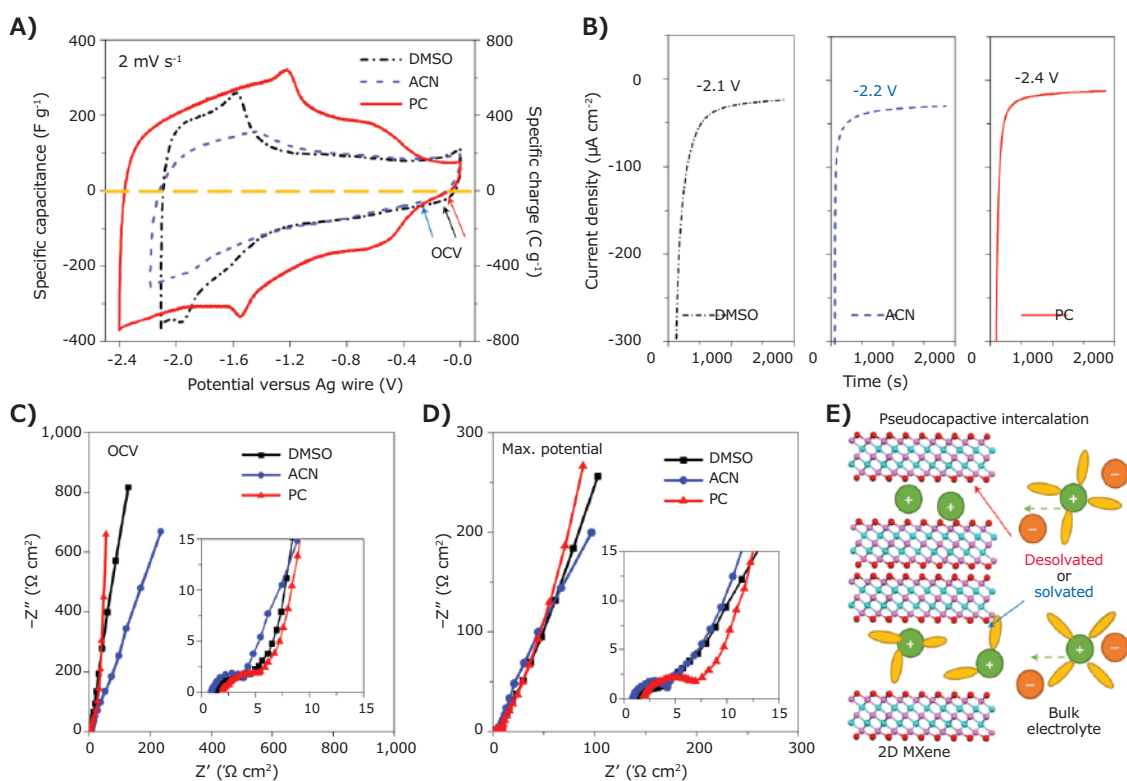


Figure 3. Macroporous $\text{Ti}_3\text{C}_2\text{T}_x$ electrode with 1M LiTFSI in DMSO, ACN and PC organic electrolytes. **A**), CV curves. The OCVs (marked by arrows) are -0.13V (black), -0.32V (blue) and -0.12V (red) versus AgCl for DMSO, ACN and PC-based electrolytes, respectively. **B**), Chronoamperometry data collected at the applied maximum potentials. **C**), EIS data collected at the OCV. **D**), EIS data collected at the maximum negative potential versus AgCl. The insets in C and D show the magnified curves in the high-frequency range; they use the same units as in C and D. **E**), Schematic of a supercapacitor using 2D MXene (pink, Ti; cyan, C; red, O) as negative electrode with solvated or desolvated states. Legend for the electrolyte: green, cation; orange, anion; yellow, solvent molecule. Adapted with permission from 10, copyright 2019 Nature.

MXenes have unique optical properties and applications, such as electrochromic devices, transparent conductors, electron transport layers, etc. Both, the thickness (n) and chemistry affect the optical absorption spectra, meaning a different MXene can be used based on specific optical needs. For example, Ti_3CNT_x was shown to exhibit thickness-dependent nonlinear saturable absorption at high light fluences, making it useful for mode-locking in fiber-based femtosecond lasers.¹³ Furthermore, a photodiode based on $\text{Ti}_3\text{C}_2\text{T}_x$ was shown to break time-reversal symmetry, achieving nonreciprocal transmission of nanosecond laser pulses.¹³ Recently, it was shown that MXenes are tunable electrochromic materials; depending on the bias used, the optical absorption peak of $\text{Ti}_3\text{C}_2\text{T}_x$ can be reversibly and controllably shifted by more than 100 nm.¹⁴ Additionally, MXenes have been used for surface-enhanced Raman spectroscopy, with calculated enhancement factors reaching 10^6 , leading to the possibility of enhanced biochemical molecular sensing.¹⁵ Due to the plasmonic nature of MXene optical properties, it is likely that they will soon find diverse optical applications spanning a wide wavelength range.

Recently, significant attention has been focused on the electronic and electromagnetic properties of MXenes due to their high electrical conductivity and processability. For example, $\text{Ti}_3\text{C}_2\text{T}_x$ was recently shown to have the highest electromagnetic

interference shielding effectiveness of all synthetic materials with comparable thickness, a $45\ \mu\text{m}$ film corresponds to 92 decibels (dB), a $2.5\ \mu\text{m}$ film gives >50 dB, and a $50\ \text{nm}$ film gives 20 dB.¹⁶ It was also shown that MXenes can be used as spray-on flexible antennas and radiofrequency identification (RFID) tags with only $\sim 100\ \text{nm}$ film thickness required.¹⁷ Some double-M MXenes (Mo, W, Ti, Zr, and Hf-based) have been proposed as topological insulators owing to the ability to use light and heavy elements simultaneously to tune the structure.¹⁸ Furthermore, a number of MXenes (Cr-, Mn-, V-, and Ti-based) are expected to exhibit ferromagnetic or antiferromagnetic properties, depending on the specific chemistry and surface terminations.¹⁹ Due to the high conductivity and surface functionalization of MXenes, it is possible to use them as gas sensors with a very high signal-to-noise ratio, and very low detection limits. For example, the limit of detection for $\text{Ti}_3\text{C}_2\text{T}_x$ was calculated to be 0.011 and 0.13 ppb for acetone and ammonia, respectively, which are some of the lowest values ever reported.² It was found that these MXene based gas sensors outperformed other 2D materials in terms of signal-to-noise ratios.²

The elastic properties of $\text{Ti}_3\text{C}_2\text{T}_x$ were studied and the Young's modulus of a single $\text{Ti}_3\text{C}_2\text{T}_x$ layer was found to be 0.33 TPa, which is the highest of any solution-processed 2D material (Figure 4).²⁰ Due to these extreme mechanical properties and

coupled with their desirable optical/electronic properties, MXenes have been widely utilized in composites. Recently, ceramic and metal matrix composites have been reported. In addition, because MXenes are water processable, polymeric composites are fabricated in polar solvents; research groups have used a variety of polymers, including polyvinyl alcohol (PVA) (Cat. Nos. **363065, 563900, 341584**), polyacrylamide (PAM) (Cat. Nos. **92560, 749222**), polyethyleneimine (PEI) (Cat. Nos. **904759, 181978**), polyethylene glycol (PEG) (Cat. No. **8.18892**), and other polymer systems.²¹ These composites have been used for a variety of applications, including electromagnetic interference shielding, electrocatalysts, electrochemical energy storage systems, and many others. In addition to polymeric composites, heterostructures have been synthesized in conjunction with other 2D and 1D materials, including graphene (Cat. Nos. **900561, 763705, 777676**), carbon nanotubes (Cat. Nos.

901046, 901082, 901056), transition metal oxides (TMOs), transition metal dichalcogenides (TMDs), and others.²² In addition to composites fabricated with polymers or other 2D materials, MXenes have also been utilized in smart fabrics. The hydrophilicity of MXenes allows them to easily coat natural fibers, such as cotton and wool, synthetics, such as polyester, and to be combined with other materials for spinning into fibers.² These composites have been used as knitted flexible supercapacitors for energy storage, as conductive fibers, and as wearable smart textiles.² Thus, by combining MXenes with other materials to form composites, the advantages of both materials can be realized. The large variety within the MXene family, coupled with the diverse families of materials with which they can be composited, leads to a massive library of possible composite systems with the ability to choose specific properties of interest.

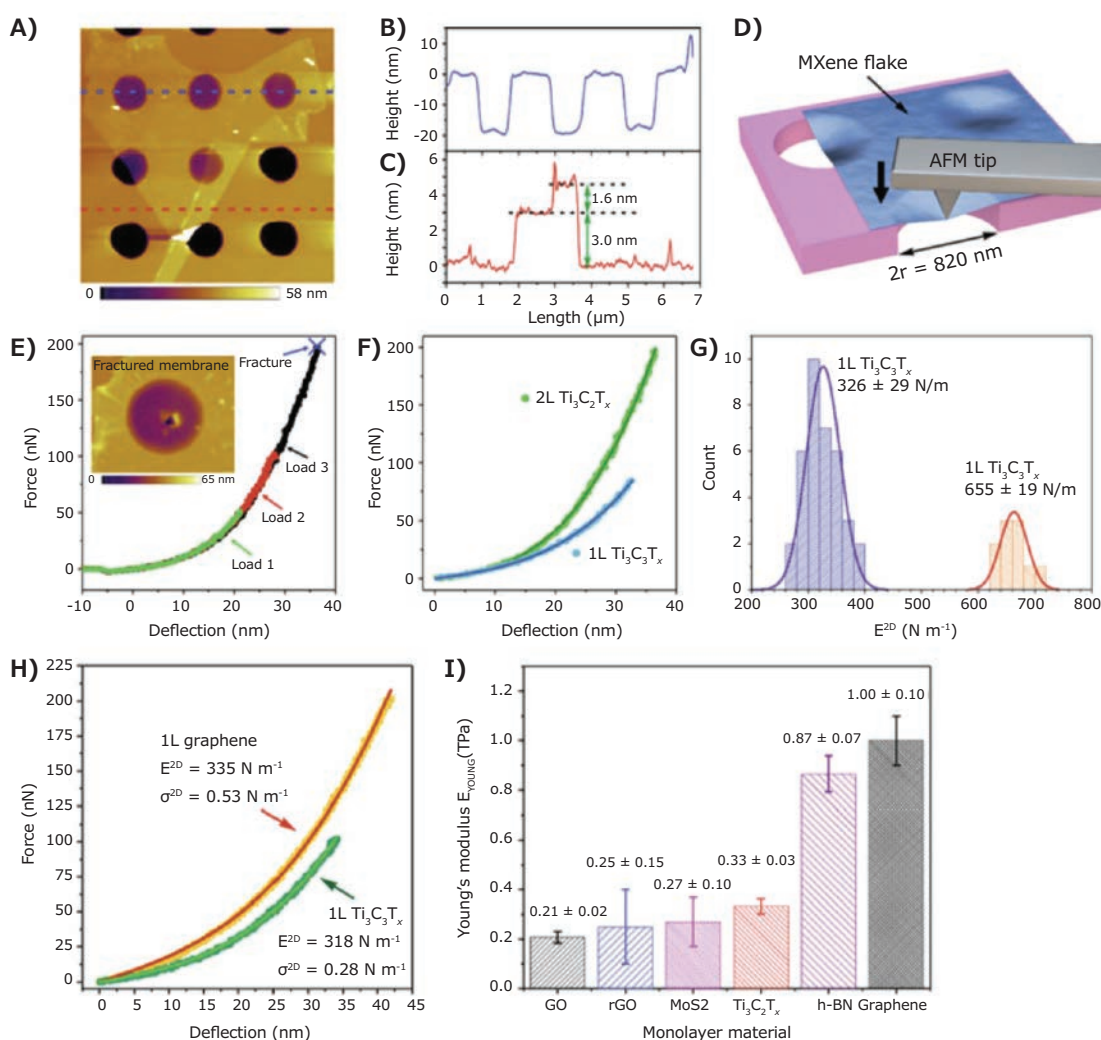


Figure 4. Mechanical measurements of monolayer and bilayer $\text{Ti}_3\text{C}_2\text{T}_x$ flakes. **A)** Noncontact AFM image of a monolayer $\text{Ti}_3\text{C}_2\text{T}_x$ flake placed over an array of microwells in a Si/SiO_2 substrate. **B,C)** Height profiles along the **B)** dashed blue and **C)** red lines shown in **A)**. **D)** Scheme of nanoindentation of a suspended $\text{Ti}_3\text{C}_2\text{T}_x$ membrane with an AFM tip. **E)** Force-deflection curves of a bilayer (2L) $\text{Ti}_3\text{C}_2\text{T}_x$ flake at different loads. The inset shows an AFM image of the fractured membrane. **F)** Comparison of loading curves for monolayer (1L) and bilayer (2L) $\text{Ti}_3\text{C}_2\text{T}_x$ membranes. Hole diameter is 820 nm. **G)** Histogram of elastic stiffness for 1L and 2L membranes. Solid lines represent Gaussian fits to the data. **H)** Comparison of experimental force-deflection curves for monolayer graphene and $\text{Ti}_3\text{C}_2\text{T}_x$ membranes. **I)** Comparison of effective Young's moduli for several 2D materials: GO, rGO, MoS_2 , h-BN, and graphene. The chart compares values produced on membranes of monolayer 2D materials in similar nanoindentation experiments. Adapted with permission from 20, copyright 2018 American Association for the Advancement of Science.

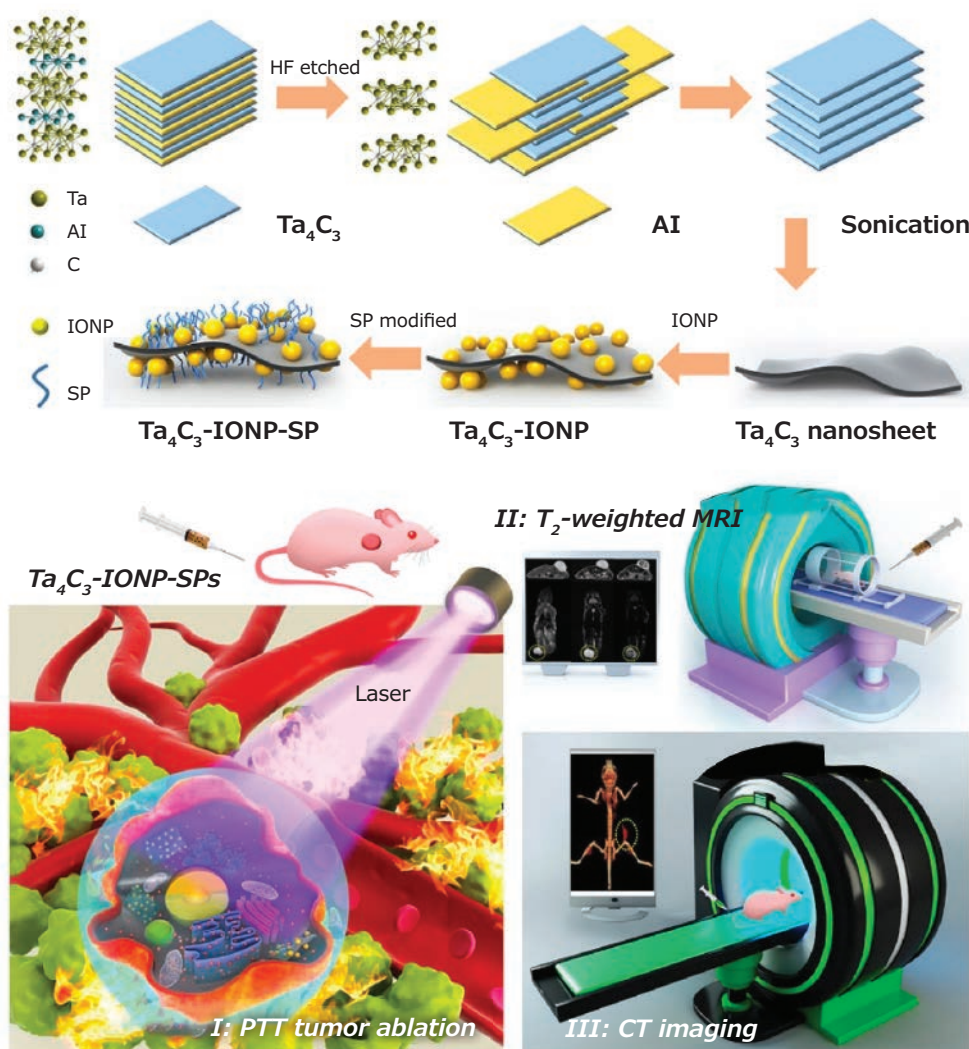


Figure 5. Schematic illustration of the fabrication process of Ta₄C₃-IONP-SPs composite nanosheets and their unique functionality for dual-modal contrast-enhanced MRI/CT imaging-guided photothermal ablation of breast cancer. Adapted with permission from 31, copyright 2018 Ivyspring.

Many research groups have begun investigating the environmental applications of MXenes, including gas separation and water purification. Due to the stacked layer morphology of MXene films, it is possible to achieve >2200 Barrer H₂ permeability with a H₂/CO₂ selectivity >160.²³ It was also shown that cations (K⁺, Na⁺, Li⁺, Ni²⁺, Ca²⁺, Mg²⁺, and Al³⁺) can be selectively filtered from water with high permeability by varying the interlayer spacing of MXene films.²⁴ Mo_{1.33}CT_x was studied for brackish and seawater desalination, showing that ion removal in seawater concentrations (600 mM NaCl) could be achieved with low energy consumption (17 kT), which is in absence of any ion exchange membranes.²⁵ It was also shown that Ti₃C₂T_x is viable for the removal of various heavy metal ions, including Cr, Pb, Cu, and others at relatively high rates.²⁶ While research into this direction is relatively recent, MXenes have demonstrated potential to play a major role in future environmental efforts.

MXenes have found promise in biomedical applications, including biosensors, antibacterial materials, in bioimaging, as therapeutics, and in theranostics (Figure 5).²⁷ The majority of biomedical applications have focused on Ti-, Nb-, and Ta-based

MXenes due to their non-toxic nature. No cytotoxicity has been observed for Ti₃C₂T_x so far. A variety of biosensors have been fabricated, focusing on detection of small molecules, including NH₃, H₂O₂, glucose, and even heavy metals. Ti₃C₂T_x has also been found to be viable for type-I photodynamic therapy-like cell killing. MXenes can also inhibit bacterial growth by imposing oxidative stress on the bacterial cell membranes. Due to the optical properties inherent in MXenes (i.e., the specific absorption spectra depend on the MXene chemistry), they can be used for bioimaging (both for photoacoustic or luminescence imaging) or as contrasting agents for computed tomography. MXenes have also been used as therapeutics for reactive oxygen species generation, as photothermal materials, and for drug cargo loading for synergistic therapy (theranostics). Two other important medical applications of MXenes include sorbents for removal urea and other toxins from blood,²⁸ as well as implantable and skin electrodes.²⁹⁻³⁰ While the applications of MXenes in the biomedical field are still relatively new, the breadth of research already conducted illustrates the variability and promise of this family for future work.

Conclusions

The unique electronic, optical, chemical and mechanical properties of MXenes coupled with the ease of processing have helped to demonstrate their tremendous promise for revolutionizing many fields. While the initial focus of MXene research has been for energy storage, their area of potential applications has since broadened to include fields ranging from smart textiles to medicine, communication, gas sensors and electrochromic devices, and in environmental remediation. Considering the growing number of discovered MXenes available, further control over the surface chemistry, better fundamental understanding of properties, and advances in MXene processing, it is likely that numerous novel applications of MXenes will also be discovered.

References

- (1) Naguib, M.; Kurtoglu, M.; Presser, V.; Lu, J.; Niu, J. J.; Heon, M.; Hultman, L.; Gogotsi, Y.; Barsoum, M. W. *Adv. Mater.* **2011**, *23* (37), 4248–4253.
- (2) Anasori, B.; Gogotsi, Y. *2D Metal Carbides and Nitrides (MXenes)*. Springer: **2019**.
- (3) Deysher, G.; Shuck, C. E.; Hantanasirisakul, K.; Frey, N. C.; Foucher, A. C.; Maleski, K.; Sarycheva, A.; Shenoy, V. B.; Stach, E. A.; Anasori, B. *ACS Nano* **2020**, *14* (1), 204–217.
- (4) Shuck, C. E.; Sarycheva, A.; Anayee, M.; Levitt, A.; Zhu, Y.; Uzun, S.; Balitskiy, V.; Zahorodna, V.; Gogotsi, O.; Gogotsi, Y. *Adv. Eng. Mater.* **2020**, *3* (22), 1901241.
- (5) Alhabeb, M.; Maleski, K.; Anasori, B.; Lelyukh, P.; Clark, L.; Sin, S.; Gogotsi, Y. *Chem. Mater.* **2017**, *29* (18), 7633–7644.
- (6) Maleski, K.; Mochalin, V. N.; Gogotsi, Y. *Chem. Mater.* **2017**, *29* (4), 1632–1640.
- (7) Gogotsi, Y.; Anasori, B. *ACS Nano* **2019**, *13* (9), 8491–8494.
- (8) Lukatskaya, M. R.; Kota, S.; Lin, Z.; Zhao, M.-Q.; Shpigel, N.; Levi, M. D.; Halim, J.; Taberna, P.-L.; Barsoum, M. W.; Simon, P.; Gogotsi, Y. *Nat. Energy* **2017**, *6*, 17105.
- (9) Anasori, B.; Lukatskaya, M. R.; Gogotsi, Y. *Nat. Rev. Mater.* **2017**, *2*, 16098.
- (10) Wang, X.; Mathis, T. S.; Li, K.; Lin, Z.; Vlcek, L.; Torita, T.; Osti, N. C.; Hatter, C.; Urbankowski, P.; Sarycheva, A.; Tyagi, M.; Mamontov, E.; Simon, P.; Gogotsi, Y. *Nat. Energy* **2019**, *4*, 241–248.
- (11) Peng, Y.-Y.; Akuzum, B.; Kurra, N.; Zhao, M.-Q.; Alhabeb, M.; Anasori, B.; Kumbur, E. C.; Alshareef, H. N.; Ger, M.-D.; Gogotsi, Y. *Energy Environ. Sci.* **2016**, *9*, 2847–2854.
- (12) Simon, P. *ACS Nano* **2017**, *11* (3), 2393–2396.
- (13) Dong, Y.; Chertopalov, S.; Maleski, K.; Anasori, B.; Hu, L.; Bhattacharya, S.; Rao, A. M.; Gogotsi, Y.; Mochalin, V. N.; Podila, R. *Adv. Mater.* **2018**, *30*, 1705714.
- (14) Salles, P.; Pinto, D.; Hantanasirisakul, K.; Maleski, K.; Shuck, C. E.; Gogotsi, Y. *Adv. Funct. Mater.* **2019**, *29* (17), 1809223.
- (15) Sarycheva, A.; Makaryan, T.; Maleski, K.; Satheeshkumar, E.; Melikyan, A. H.; Minassian, H.; Yoshimura, M.; Gogotsi, Y. *J. Phys. Chem. C* **2017**, *121* (36), 19983–19988.
- (16) Shahzad, F.; Alhabeb, M.; Hatter, C. B.; Anasori, B.; Hong, S. M.; Koo, C. M.; Gogotsi, Y. *Science* **2016**, *353* (6304), 1137–1140.
- (17) Sarycheva, A.; Polemi, A.; Liu, Y.; Dandekar, K.; Anasori, B.; Gogotsi, Y. *Sci. Adv.* **2018**, *4* (9), eaau0920.
- (18) Khazaeli, M.; Ranjbar, A.; Arai, M.; Sasaki, T.; Yunoki, S. *J. Mater. Chem. C* **2017**, *5*, 2488–2503.
- (19) Kumar, H.; Frey, N. C.; Dong, L.; Anasori, B.; Gogotsi, Y.; Shenoy, V. B. *ACS Nano* **2017**, *11* (8), 7648–7655.
- (20) Lipatov, A.; Lu, H.; Alhabeb, M.; Anasori, B.; Gruverman, A.; Gogotsi, Y.; Sinitiski, A. *Sci. Adv.* **2018**, *4* (6), eaat0491.
- (21) Ng, V. M. H.; Huang, H.; Zhou, K.; Lee, P. S.; Que, W.; Xu, J. Z.; Kong, L. B. *J. Mater. Chem. A* **2017**, *5*, 3039–3068.
- (22) Pomerantseva, E.; Gogotsi, Y. *Nat. Energy* **2017**, *2*, 17089.
- (23) Ding, L.; Wei, Y.; Li, L.; Zhang, T.; Wang, H.; Xue, J.; Ding, L.-X.; Wang, S.; Caro, J.; Gogotsi, Y. *Nat. Commun.* **2018**, *9* (1), 155.
- (24) Ren, C. E.; Hatzell, K. B.; Alhabeb, M.; Ling, Z.; Mahmoud, K. A.; Gogotsi, Y. *J. Phys. Chem. Lett.* **2015**, *6* (20), 4026–4031.
- (25) Srimuk, P.; Halim, J.; Lee, J.; Tao, Q.; Rosen, J.; Presser, V. *ACS Sustain. Chem. Eng.* **2018**, *6* (3), 3739–3747.
- (26) Wu, Y.; Pang, H.; Liu, Y.; Wang, X.; Yu, S.; Fu, D.; Chen, J.; Wang, X. *Environ. Pollut.* **2019**, *246*, 608–620.
- (27) Huang, K.; Li, Z.; Lin, J.; Han, G.; Huang, P. *Chem. Soc. Rev.* **2018**, *47*, 5109–5124.
- (28) Meng, F.; Seredych, M.; Chen, C.; Gura, V.; Mikhalovsky, S.; Sandeman, S.; Ingavle, G.; Ozulumba, T.; Miao, L.; Anasori, B. *ACS Nano* **2018**, *12* (10), 10518–10528.
- (29) Driscoll, N.; Richardson, A. G.; Maleski, K.; Anasori, B.; Adewole, O.; Lelyukh, P.; Escobedo, L.; Cullen, D. K.; Lucas, T. H.; Gogotsi, Y. *ACS Nano* **2018**, *12* (10), 10419–10429.
- (30) Driscoll, N.; Maleski, K.; Richardson, A. G.; Murphy, B.; Anasori, B.; Lucas, T. H.; Gogotsi, Y.; Vitale, F. J. *Vis. Exp.* **2020**, *156*, e60741.
- (31) Liu, Z.; Lin, H.; Zhao, M.; Dai, C.; Zhang, S.; Peng, W.; Chen, Y. *Theranostics* **2018**, *8* (6), 1648–1664.

MXene Precursor-MAX Phases

Name	Description	Cat. No.
Titanium Aluminium Carbide 211	≤ 40 micron	910759-25G
	≤ 100 micron	910821-25G
	≤ 200 micron	910708-25G
Titanium Aluminium Carbide 312	≤ 40 micron	910775-25G
	≤ 100 micron	910767-25G
	≤ 200 micron	910740-25G

Etchants

Name	Purity	Form	Cat. No.
Buffer HF improved	-	liquid	901657-1L
Buffer HF improved	with surfactant	liquid	901667-1L
Hydrochloric acid	99.999% trace metals basis	liquid	339253-100ML 339253-500ML 339253-6X500ML
Hydrofluoric acid	≥99.99% trace metals basis	liquid	339261-100ML 339261-4X100ML 339261-800ML
Hydrofluoric acid	≥48%	liquid	30107-500ML 30107-1L 30107-6X1L 30107-5L

Name	Purity	Form	Cat. No.
Hydrofluoric acid	≥40%	liquid	30103-1L 30103-6X1L 30103-2.5L 30103-5L
Hydrofluoric acid	48%	liquid	695068-25ML 695068-500ML
Lithium fluoride	99.995%	fused (pieces)	668052-10G 668052-25G 668052-100G
Lithium fluoride	99.995%	powder	669431-50G
Lithium fluoride	≥99.99% trace metals basis	powder and chunks	449903-2G 449903-10G
Lithium fluoride	≥99.98% trace metals basis	powder	203645-5G 203645-25G
Lithium fluoride	-	powder	237965-100G 237965-1KG

Graphene and Graphite

CVD Graphene

Name	Description	Cat. No.
Monolayer graphene film	4 in diameter on copper foil	900415-1EA
	1 cm x 1 cm on copper foil, with PMMA coating	900443-4EA
	1 in x 1 in on copper foil, with PMMA coating	900445-1EA
	1 cm x 1 cm on quartz	773719-4EA
	1 cm x 1 cm on copper foil	773697-4EA
	1 in x 1 in on copper foil	799009-1EA
	1 cm x 1 cm on SiO ₂ /Si substrate	773700-4EA
	1 in x 1 in on PET film	745863-1EA 745863-5EA
	2 in x 2 in on PET film	745871-1EA

Graphene Oxide and Graphene Powders

Name	Description	Cat. No.
Carboxylated reduced graphene oxide	carboxylic acid enriched, dispersible reduced graphene oxide-	910406-200MG
Graphene	electrical conductivity > 10 ³ S/m	900561-500MG
	amine functionalized	900551-250MG
	silane modified	900552-250MG
Graphene nanoplatelets	surface area: 2.0-2.25 g/cm ³	900407-250G
Sulfonated reduced graphene oxide	sulfate group enriched, highly dispersible reduced graphene oxide, sodium salt	909130-500MG

Graphite

Name	Description	Cat. No.
Graphite anode powder	Electrochemistry performance: • Reversible capacity: 355 mAh/g • Irreversible capacity: 23 mAh/g • First cycle efficiency: 93.7%.	907154-500G
	High Precision Coulometry (HPC) • Standard 2.2 Ah 18650 Cells • Coulombic efficiency > 0.998 at 40 Celsius	
Graphite dispersion	1.0mg/mL in acetone-water Capacity: 400-450 mAh/g (3-15 graphene layers)	902942-500ML
	Capacity: 250 - 400 mAh/g (8-30 layers)	902926-500ML

2D Nanomaterial Inks and Powders

Exfoliated Hexagonal Boron Nitride Inks

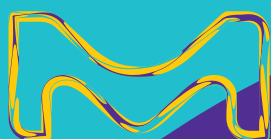
Name	Description	Cat. No.
Hexagonal boron nitride ink	Solid content : 20-40% for blade coating	901349-10ML
	Solid content : 4.4-6.4% for inkjet printing	901410-5ML

Graphene Inks

Name	Description	Cat. No.
Graphene ink	for inkjet printing with ethyl cellulose in cyclohexanone and terpineol, inkjet printable	793663-5ML
	for gravure printing with ethyl cellulose in terpineol, gravure printable	796115-10ML
	for screen printing with ethyl cellulose in terpineol, screen printable	798983-10ML
	for inkjet printing photonicallly annealable	900695-5ML
Graphene ink for spin/spray coating photonicallly annealable	prepared by spin-coating at 2000 rpm/30 s for 5 coats, followed by thermal annealing at 300 °C in air for 30 minutes	900960-10ML
Graphene ink in water	flexo/gravure/screen printable	805556-10ML
	inkjet printable	808288-5ML
	screen printable	808261-10ML

Molybdenum Disulfide Inks

Name	Description	Cat. No.
Molybdenum disulfide ink for inkjet printing	Resistivity: 10-100 kΩ-cm (thermally annealed 400 °C for 3 hours in Ar/H ₂ environment, film thickness >150 nm)	901187-5ML
Molybdenum disulfide ink for spin/spray coating	Resistivity: 75-100 kΩ-cm (Prepared by spin-coating at 1000 rpm/30 s for 1 coat, followed by thermal annealing at 400°C in Ar/H ₂ for 3 hours)	901867-10ML



subscribe today

Don't miss another topically focused technical review.

It's **free** to sign up for a print or digital subscription of *Material Matters*™.

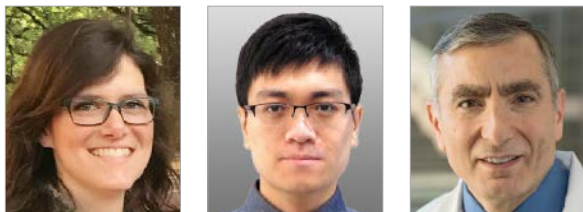
- Advances in cutting-edge materials
- Technical reviews on emerging technology from leading scientists
- Peer-recommended materials with application notes
- Product and service recommendations

MILLIPORE
SIGMA



To view the library of past issues or to subscribe, visit
SigmaAldrich.com/mm

Synthesis and Applications of Graphene Nanoribbons Synthesized via Top-Down Methods



Emily McHugh,¹ Tuo Wang,¹ and James M. Tour^{1,2,3*}

¹Department of Chemistry, ²Smalley-Curl Institute and The NanoCarbon Center, ³Department of Materials Science and NanoEngineering, Rice University, 6100 Main Street MS 222, Houston, Texas 77005, USA
*Email: tour@rice.edu

Introduction

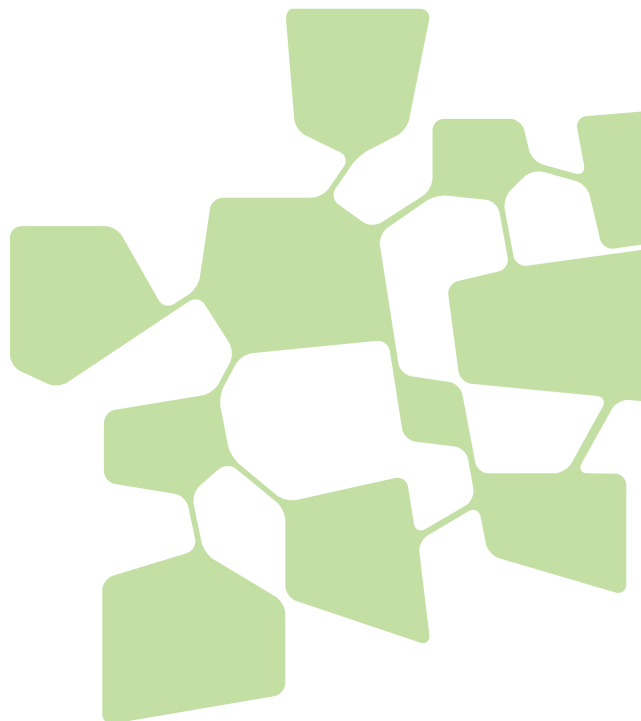
Graphene nanoribbons (GNRs) are quasi one-dimensional narrow strips of graphene comprised of sp^2 -hybridized carbon atoms arranged into hexagonal honeycomb lattice configurations. The high aspect ratio, abundant edges, conductivity, and propensity for functionalization make GNRs an attractive material that draws interest from a wide range of fields, including chemistry, physics, materials science, and biology. GNRs have already found use in various applications such as sensors, conductive films, polymer composites, batteries, energy-conversion/storage devices, bioimaging, DNA sequencing, and neurophysiological recovery. Here, we will review the prevalent top-down synthetic methods to GNRs, as well as the current applications for these materials.

Top-Down Synthesis of GNRs from Unzipping of Nanotubes

Bottom-up and top-down methods are both currently used for the synthesis of GNRs. Bottom-up approaches allow for the synthesis of precise narrow ribbons due to the controllable assembly of small molecule building blocks.¹⁻² Although this method results in high-quality GNRs with minimal defects, the scalability of GNR synthesis via this route is less feasible; therefore, top-down methods are preferred when lower-cost mass-production is desired. Such top-down approaches often involve the longitudinal unzipping of multi-walled carbon nanotubes (MWCNTs) to produce GNRs that are as long as the starting MWCNTs had been. Redox chemistry is commonly used for such longitudinal splitting of MWCNTs with many publications reporting successful GNR fabrication under both reductive

and oxidative conditions. The former typically employs the use of potassium (K) vapor or sodium-potassium alloy (Na/K) reducing agents whereas the latter uses oxidizing agents, such as potassium permanganate (KMnO₄) or ammonium persulfate (NH₄)₂S₂O₈.³⁻⁸ Each method of GNR synthesis necessitates the use of low-defect MWCNTs since defects act as termination sites that prevent completion of the unzipping reaction.

Both the reductive splitting of MWCNTs by K vapor and the solution-based Na/K methods were developed by the Tour group.³⁻⁴ In the former, MWCNTs are exposed to K in the vapor phase by heating the two together in a sealed glass tube to 250 °C for 14 h;³ however, the solution-based approach has greater utility. In that, GNRs are obtained by suspending MWCNTs in 1,2-dimethoxyethane (DME) (**Cat. No. 259527**) followed by the addition of Na/K alloy (2:9 molar ratio). The reaction mixture is allowed to stir at room temperature for 3 d before the product and excess reagents are quenched and purified. All synthetic steps are performed under inert atmosphere.⁴ In this process, K atoms intercalate within the interstices of the concentric MWCNT walls, resulting in blistering around the metal atoms and longitudinal cracking of the walls. The presumed aryl radicals receive another electron from the metal to form the aryl anions. Since the carbon atoms found along the edges at which the cleft in the sidewall is formed are in the reduced carbanionic state, the edge carbon atoms are highly reactive and are prone to electrophilic attack. The carbanions can either be quenched via the addition of MeOH to produce protonated



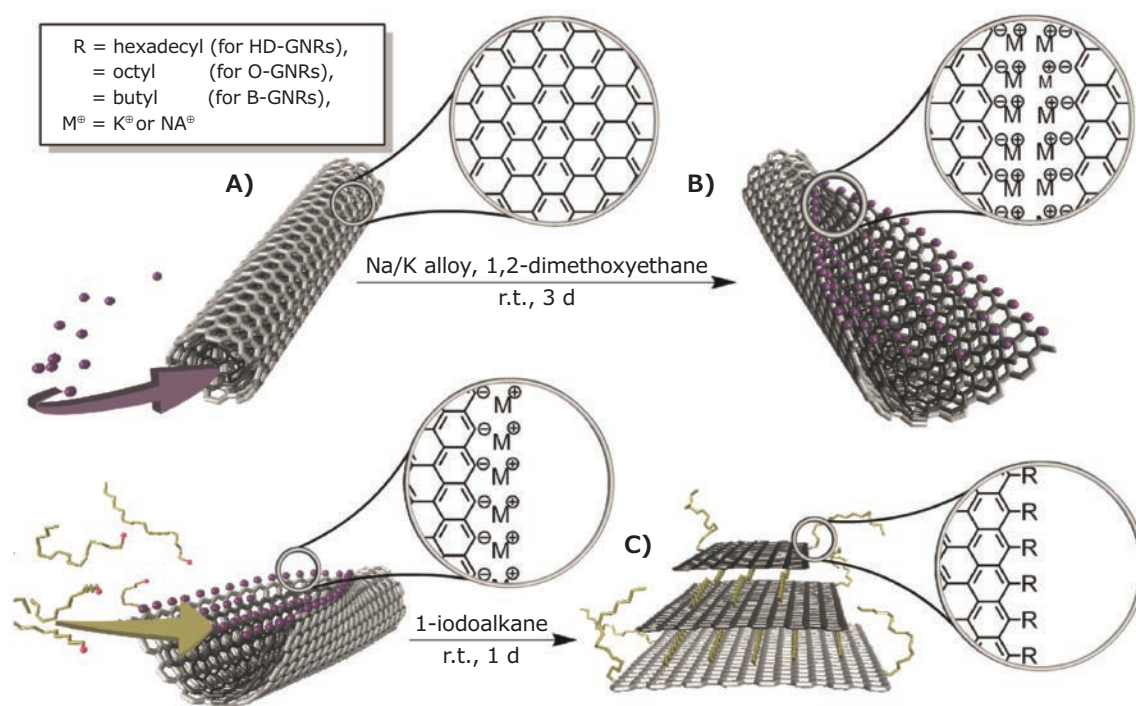


Figure 1. Reductive intercalation-driven synthesis of alkyl functionalized GNRs. **A)** The MWCNT is split by the intercalation of K between the walls of the nanotube due to strain along the carbon-carbon bonds induced by the metal atoms. **B)** Carbanions are formed along the nanoribbon edge after splitting of the MWCNT walls. **C)** Functionalization of the GNRs with alkyl moieties: the same process is used for the synthesis of H-terminated GNRs or PEG-GNRs, but MeOH or ethylene oxide are added during the second step, respectively, instead of 1-iodoalkane. Reprinted with permission from reference 4, copyright 2012 American Chemical Society.

(H-terminated) GNRs or functionalized with varying moieties, depending on the targeted properties of the material (**Figure 1**). For example, edge functionalization of the GNRs with alkyl or poly(ethylene glycol) (PEG) moieties has shown to significantly improve the dispersibility of GNRs in organic or aqueous solvents, respectively, while leaving the basal planes intact. By preserving the sp^2 -hybridized basal plane, the conductivity of the GNRs is retained while altering the chemical properties at the edges through functionalization, allowing for increased dispersibility and interfacial interactions of the functionalized GNRs with other materials. Such interactions are advantageous for the production of composites. For instance, conductive fillers can leverage the high aspect ratio and conductivity of the functionalized GNRs to achieve smaller mass loadings while still providing percolation. It should be noted that although GNRs synthesized via reductive-intercalation assisted unzipping are highly conductive, the strong van der Waals forces between the GNR stacks present a challenge for effectively exfoliating the material into monolayer ribbons.

In 2009, the Tour group established a method for oxidatively splitting MWCNTs to form GNRs reminiscent of synthesizing graphene oxide (GO) from graphite by the Hummer's method. This top-down method consists of dispersing in concentrated H_2SO_4 followed by the addition of $KMnO_4$. The reaction mixture is stirred at room temperature for 1 h and then heated at 55–70 °C for 1 h.⁵ Once purified, the resulting product is highly soluble

in a wide range of solvents including water, ethanol, and various polar organic solvents. Unlike GNRs synthesized by reductive splitting, oxidatively produced GNRs are readily exfoliated due to the carboxylate anionic charges, allowing for single-layer ribbons to be acquired. However, this ease of exfoliation comes at the expense of reduced conductivity of the GNR product since the sp^2 -hybridization of the basal plane is lost due to defects induced by the oxidation reaction. Initially, this process was thought to be driven by oxidative chemical-bond cleavage.⁵ This mechanism has since been revised to one proposing intercalation-driven unzipping similar to the reductive splitting method. Three consecutive steps occur: (1) intercalation-unzipping of the MWCNT precursor, (2) oxidation of the nanoribbons, and (3) exfoliation of the multilayer GNR stacks (**Figure 2**).⁶ Molecules of H_2SO_4 intercalate between the walls of the MWCNT via entrance through the opened ends of the nanotubes or through vacancy defects that are already present in the walls. The intercalated H_2SO_4 causes outward radial expansion of the nanotube that induces unzipping to the foliated GNR product. Following successful unzipping of the nanotubes, oxidation of the edges and basal plane of the GNRs can occur. The oxidized GNR stacks can then be exfoliated upon exposure to water. By altering the ratio of $KMnO_4$ /MWCNT (by weight) or the reaction duration, it was determined that the oxidative splitting reaction can be terminated at any of the aforementioned steps. Therefore, the reaction conditions can be controlled to produce GNRs with

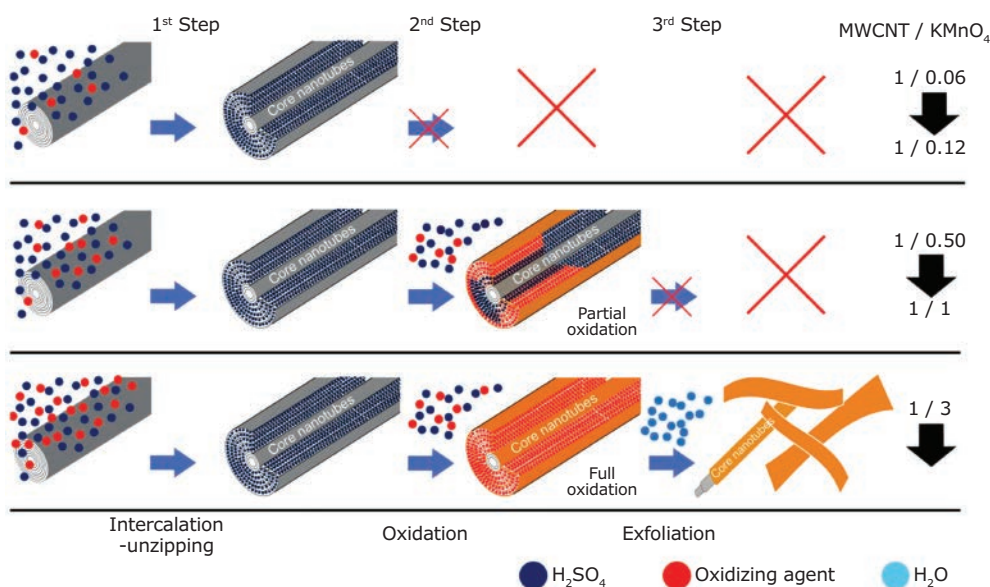


Figure 2. Mechanism of unzipping MWCNTs by oxidizing agents. The oxidative splitting of MWCNTs occurs in three consecutive steps: intercalation-unzipping, oxidation, and exfoliation. Since each step occurs sequentially, the reaction can be terminated at any step by controlling the reaction conditions (ratio by weight of MWCNT/KMnO₄). GNRs ranging from non-oxidized (gray color of MWCNT wall) to heavily oxidized (red color of MWCNT wall) can be produced, allowing desired properties of the nanoribbons to be targeted (i.e. conductivity or effective dispersibility in water or organic solvents). Reprinted with permission from reference 6, copyright 2018 American Chemical Society.

varying properties, ranging from non-oxidized multilayered GNR products with uncompromised conductivity to heavily oxidized single-layer GNRs with facile dispersion in water but lower conductivity. To produce GNRs by oxidative splitting without sacrificing conductivity, milder oxidants can be used instead of KMnO₄. For instance, (NH₄)₂S₂O₈ (**Cat. No. 215589**) has shown to be effective at unzipping MWCNTs without introducing a significant number of oxygen defects along the graphene basal plane. This unzipping protocol calls for the suspension of MWCNTs in a mixture of oleum (**Cat. No. 435597**) and concentrated H₂SO₄ (**Cat. No. 339741**) (1:1 ratio by volume) prior to the addition of (NH₄)₂S₂O₈ and heating under reflux at 80 °C for 1 d.^{7,8}

Application of GNRs for Neurophysiological Recovery

We have conducted a study which shows that nontoxic poly(ethylene glycol) graphene nanoribbons (PEG-GNRs) generate a permissive microenvironment for spinal cord recovery after injury (**Figure 3**).⁹ GNRs are functionalized with PEG via reductive splitting of MWCNTs followed by subsequent anionic polymerization with ethylene oxide, rendering a product with water-soluble PEG moieties that emanate from the edges of the GNR. The edge functionalization of the GNRs maintains the pristine basal planes and, therefore, the electrical conductivity of the carbon core. Since these basal planes are highly electrically conductive, neuronal growth can be stimulated along the graphene-based material.⁹⁻¹² The primary structural components of PEG-GNRs provide a permissive microenvironment conducive for spinal cord recovery; the composite material spans the gap

between severed axons, forming a nanoscaffold capable of facilitating the conduction of neuronal signals across the lesion while permitting growth along the framework.^{9,13-14} Thus far, we have shown in 5 rats that the application of 0.5 mL of 1% PEG-GNRs solution in PEG600 (**Cat. No. 8.07486**) at C5 after complete cervical transection resulted in ~30% restoration, of the pre-surgery somatosensory evoked potential (SSEP) amplitude within 24 h. One animal with no SSEP measurements regained mobility of its forelimbs and hindlimbs within two weeks after surgery, and scored 19 out of 21 by week three on the Basso, Beattie, and Bresnahan (BBB) motility scale (**Figure 3**).¹⁴ This can be seen in an online video.¹⁵

Applications of GNRs in Batteries

The high aspect ratio of GNRs enables them to provide percolation at a lower mass loading than other carbon species such as carbon black, graphene nanoplatelets, and graphite. This property has made GNRs a good candidate for a conductive filler in batteries. Over the past decade, many papers using GNRs in batteries have been published.¹⁶⁻¹⁸

We have used GNRs, polyacrylonitrile, and sulfur to make a sulfurized carbon (SC) cathode to pair with Li-metal anodes (**Figure 4**).¹⁶ The full battery (FB) based on the graphene-carbon nanotube-Li (GCNT-Li)/SC cathode is demonstrated with high energy density (752 Wh kg⁻¹ total electrodes, where total electrodes = GCNT-Li + SC + binder), high areal capacity (2 mAh cm⁻²), and cyclability (80% retention at >500 cycles) and is free of Li polysulfides and dendrites that would cause severe capacity fade.

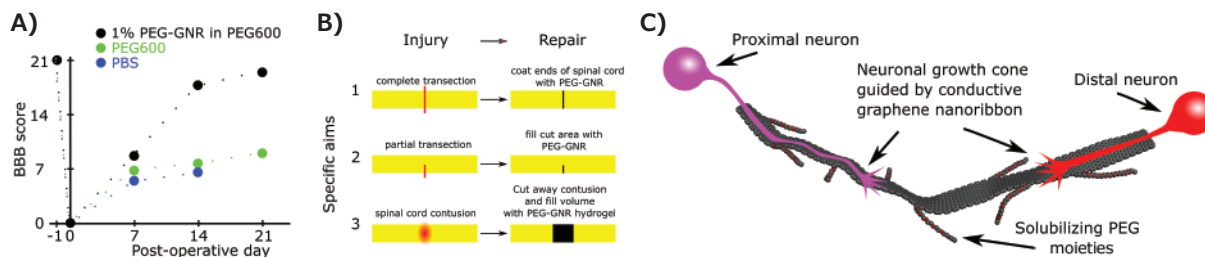


Figure 3. A) Mobility recovery of a single rat following intra-topical application of 1% PEG-GNRs in PEG600 to blunt ends of transected spinal cord compared to PEG600 alone and PBS alone. Dashed lines guide the eye. B) Yellow bar represents the spinal cord, red represents cut or injured area, and black represents area where PEG-GNRs have been applied. C) Postulated mechanism of repair: PEG-GNRs provide a microenvironment where growth is encouraged, and the conductive nature of the graphene allows neurons to communicate with each other over a distance and grow towards each other along the nanoribbon scaffold.

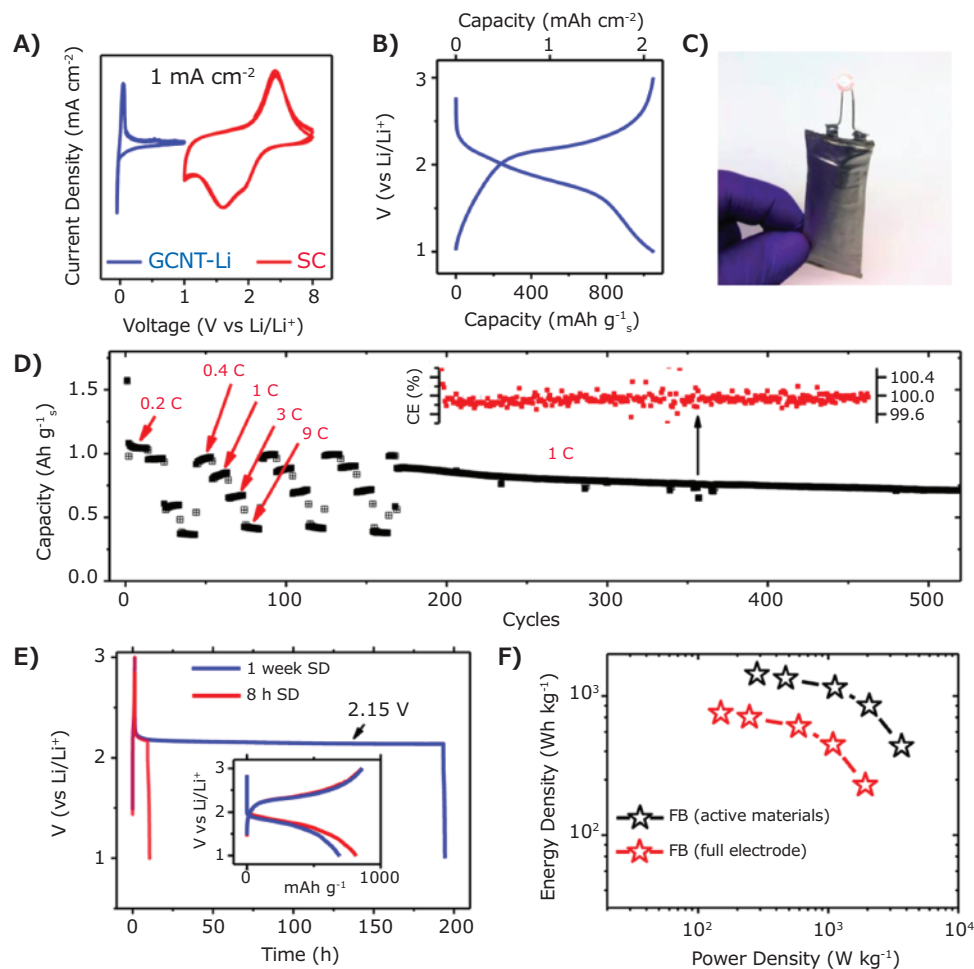


Figure 4. Measurements in a full battery with a GCNT-Li anode and SC cathode. A) CVs of GCNT-Li and SC cathode half-cells in 4 M LiFSI/DME at 0.5 mV s⁻¹. B) Galvanostatic charge/discharge curves of the FB at 0.1 C with areal capacity of 2 mAh cm⁻². C) Photograph of a FB prototype powering a LED. D) Sequential rate performance test (0.2 to 9 C) and cycling stability of the FB. Inset: CE (%) of the rate and stability test. The reference blue dashed line is set to 99.9%. E) Self-discharge (SD) tests of the FB after 8 h and 1 week showing charge curve followed by continuous discharge curve during and after the open circuit period. Inset: Voltage vs capacity of the SD tests. F) Ragone plot of the GCNT-Li/SC FB, here considering the combined mass of the anode and cathode active materials (Li and S) and the full electrode mass (including binder, carbon additives, GCNT, excess of Li), excluding the current collector. Reprinted with permission from reference 16, copyright 2017 American Chemical Society.

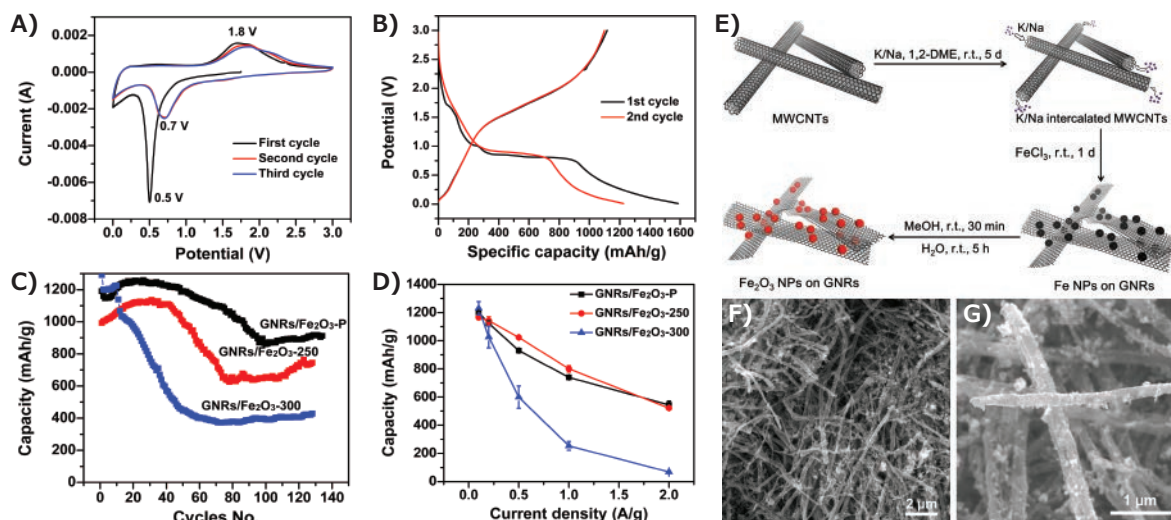


Figure 5. Electrochemical properties of GNR/ Fe_2O_3 composite anode electrodes. All of the capacities shown here are based on the weight of iron oxide NPs. **A)** Cyclic voltammetry of the GNR/ Fe_2O_3 -P composite anode. **B)** The first and second charge-discharge curves of the composite GNR/ Fe_2O_3 -P anode. **C)** Comparison of the cyclability of GNR/ Fe_2O_3 -P, GNR/ Fe_2O_3 -250, and GNR/ Fe_2O_3 -300 at a rate of 0.2 A/g. **D)** Comparison of rate performance of GNR/ Fe_2O_3 -P, GNR/ Fe_2O_3 -250, and GNR/ Fe_2O_3 -300. **E)** Scheme of the synthesis of the GNR/ Fe_2O_3 composites. **F)** Low magnification scanning electronic microscope (SEM) image of the GNR/ Fe_2O_3 -P composites. **G)** High magnification SEM image of the GNR/ Fe_2O_3 -P composites. Reprinted with permission from reference 17, copyright 2017 Wiley.

We have also developed a composite material from graphene nanoribbons and iron oxide nanoparticles that provides a remarkable route to lithium-ion battery anodes with high specific capacity and cycle stability.¹⁷ At a rate of 100 mA/g, the material exhibits a high discharge capacity of ~ 910 mAh/g after 134 cycles, which is $>90\%$ of the theoretical Li-ion storage capacity of iron oxide (**Figure 5**). Utilizing graphene nanoribbons as a conductive platform on which iron oxide nanoparticles are formed combines the advantages of long carbon nanotubes and flat graphene surfaces (**Figure 5**). The high capacity over prolonged cycling achieved is due to the synergy between electrically percolating networks of conductive graphene nanoribbons and the high lithium-ion storage capability of iron oxide nanoparticles.

Apart from conventional Li-ion battery anodes, we have designed an asphalt-derived (Asp) porous carbon-graphene nanoribbon (Asp-GNR) composite material as a substrate for Li plating in Li metal anodes.¹⁸ GNRs were added to enhance the conductivity of the host material at high current densities to produce Asp-GNR-Li. Asp-GNR-Li has demonstrated remarkable rate performance from 5 A/g Li (1.3C) to 40 A/g Li (10.4C) with Coulombic efficiencies of $>96\%$ (**Figure 5**). Stable cycling was achieved for more than 500 cycles at 5 A/g Li, and the areal capacity reached up to 9.4 mAh/cm² at a maximum discharging/charging rate of 20 mA/cm² that was $10\times$ faster than that of typical LIBs, suggesting utility in ultrafast charging systems.

Applications of GNRs for Deicing

High conductivity also makes GNRs a promising material for deicing and anti-icing devices. Owing to the carbon anions generated during the reductive splitting process, GNRs can be easily functionalized on the edge to become superhydrophobic. In a previous work, we have designed a perfluorododecylated graphene nanoribbon (FDO-GNR) film that takes advantage of both the low polarizability of perfluorinated carbons and the intrinsic conductive nature of graphene nanoribbons (**Figure 6**).¹⁹ The FDO-GNR films are superhydrophobic with a sheet resistance below 8 k Ω /sq and exhibit an anti-icing property that prevents freezing of incoming ice-cold water down to -14 °C. At lower temperatures, voltage can be applied to the films to resistively heat and deice the surface. A spray-coating method makes this method suitable for large-scale applications. The anti-icing and deicing properties render the FDO-GNR films promising for use in extreme environments.

In another work, we demonstrated a GNR-epoxy composite for deicing the surface of rotor blades.²⁰ A conductive composite of GNR stacks and epoxy was prepared. The epoxy is filled with the GNR stacks, which serve as a conductive additive. The GNR stacks are, on average, 30 nm thick, 250 nm wide, and 30 μm long. This GNR-filled epoxy composite exhibits a conductivity of >100 S/m at 5 wt% GNR content, which permits application of the GNR-epoxy composite for deicing of surfaces through Joule (voltage-induced) heating generated by the voltage across the composite. A power density of 0.5 W/cm² was delivered to remove ~ 1 cm-thick (14 g) monolith of ice from a static helicopter rotor blade surface in a -20 °C environment.

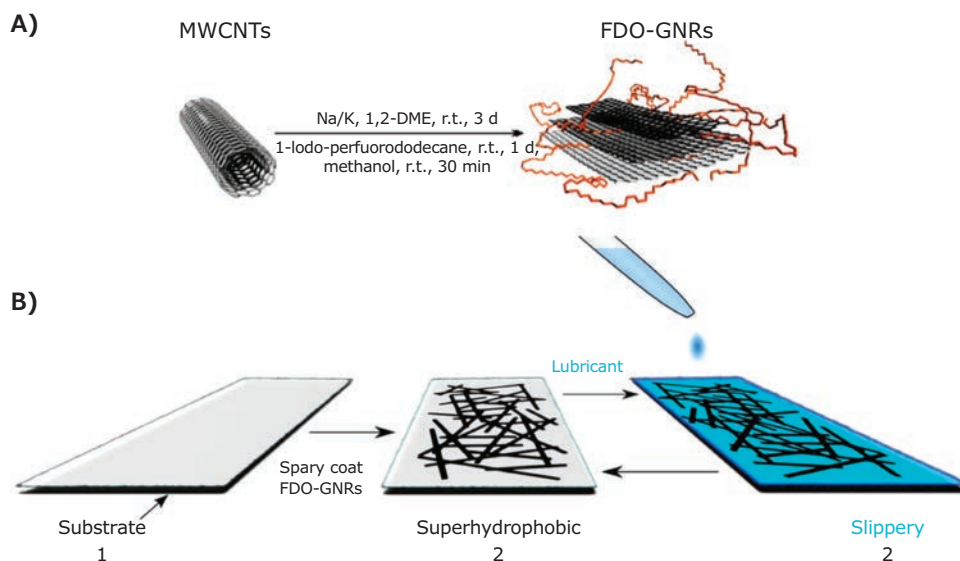


Figure 6. A) Schematic illustration of the synthesis of FDO-GNRs and B) fabrication of FDO-GNR films. Reprinted with permission from reference 19, copyright 2016 American Chemical Society.

Conclusion

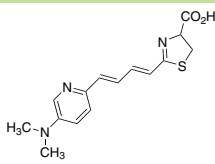
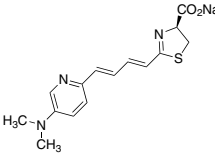
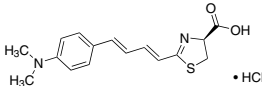
The cost-effective and facile production of GNRs synthesized by either reductive or oxidative unzipping of nanotubes makes high production rates more feasible. This increases the practicality of utilizing these GNRs in numerous applications, primarily ones associated with lithium-ion batteries, conductive thin films, and polymer composites; however, even more promising would be the mass production of a conductive nanoscaffold therapeutic device for the restoration of mobility after spinal cord injury. Owing to the unique and facile tunability of the GNR properties, the potential breadth and depth of applicability for these quasi, one-dimensional graphene structures are exceedingly broad and capable of crossing a multitude of fields.

References

- (1) Long, C.; Hernandez, Y.; Feng, X.; Müllen, K. *Angew. Chem. Int. Ed.* **2012**, *51*, 7640–7654.
- (2) Cai, J.; Ru eux, P.; Jaafar, R.; Bieri, M.; Braun, T.; Bankenburg, S.; Muoth, M.; Seitsonen, A. P.; Saleh, M.; Feng, X.; Müllen, K.; Fasel, R. *Nature* **2010**, *466*, 470–473.
- (3) Kosynkin, D. V.; Lu, W.; Sinitskii, A.; Pera, G.; Sun, Z.; Tour, J. M. *ACS Nano* **2011**, *5* (2), 968–974.
- (4) Genorio, B.; Lu, W.; Dimiev, A. M.; Zhu, Y.; Raji, A. R. O.; Novosel, B.; Alemany, L. B.; Tour, J. M. *ACS Nano* **2012**, *6* (5), 4231–4240.
- (5) Kosynkin, D. V.; Higginbotham, A. L.; Sinitskii, A.; Lomeda, J. R.; Dimiev, A.; Price, B. K.; Tour, J. M. *Nature* **2009**, *458* (7240), 872–876.
- (6) Dimiev, A. M.; Khannanov, A.; Vakhitov, I.; Kiliamov, A.; Shukina, K.; Tour, J. M. *ACS Nano*, **2018**, *12* (4), 3985–3993.
- (7) Tour, J. M.; Dimiev, A. Production of graphene nanoribbons by oxidative anhydrous acidic media, U.S. Patent 20150307357A1, Oct 29, 2015.
- (8) Wang, T.; Wang, Z.; Salvatierra, R. V.; McHugh, E.; Tour, J. M. *Carbon*, **2020**, *158*, 615–623.
- (9) Sikkema, W. K. A.; Metzger, A. B.; Wang, T.; Tour, J. M. *Surg. Neurol. Int.* **2017**, *8*, 84.
- (10) Akhavan, O.; Ghaderi, E. J. *Mater. Chem. B* **2013**, *1*, 6291–6301.
- (11) Sahni, D.; Jea, A.; Mata, J. A.; Marcano, D. C.; Sivaganesan, A.; Berlin, J. M.; Tatsui, C. E.; Sun, Z.; Luerssen, T. G.; Meng, S.; Kent, T. A.; Tour, J. M. *J. Neurosurg. Pediatr.* **2013**, *11*, 575–583.
- (12) Palejwala, A. H.; Fridley, J. S.; Mara, J. A.; Samuel, E. L.; Luerssen, T. G.; Perlaky, L.; Kent, T. A.; Tour, J. M.; Jea, A. *Surg. Neurol.* **2016**, *7*, 75.
- (13) Kim, C. Y.; Sikkema, W. K. A.; Kim, J.; Kim, J. A.; Walter, J.; Dieter, R.; Chung, H. M.; Mana, A.; Tour, J. M.; Canavero, S. *Neural. Regen. Res.* **2018**, *13*, 1440–1446.
- (14) Kim, C. Y.; Sikkema, W. K. A.; Hwang, I. K.; Oh, H.; Kim, U. J.; Lee, B. H.; Tour, J. M. *Surg. Neurol. Int.* **2016**, *7*, 632–636. Raji, A.-R. O.; Salvatierra, R. V.; Kim, N. D.; Fan, X.; Li, Y.; Silva, G. A. L.; Sha, J.; Tour, J. M. *ACS Nano* **2017**, *11*, 6362–6369.
- (15) Sikkema, W. Recovery of paralyzed rodent by using TexasPEG [Video File]. *YouTube*, Mar 17, 2017. https://www.youtube.com/watch?time_continue=2&v=nPuYq1JrLCQ (accessed Nov 4, 2019).
- (16) Raji, A.-R. O.; Salvatierra, R. V.; Kim, N. D.; Fan, X.; Li, Y.; Silva, G. A. L.; Sha, J.; Tour, J. M. *ACS Nano* **2017**, *11*, 6362–6369.
- (17) Lin, J.; Raji, A.-R. O.; Nan, K.; Peng, Z.; Yan, Z.; Samuel, E. L. G.; Natelson, D.; Tour, J. M. *Adv. Funct. Mater.* **2014**, *24*, 2044–2048.
- (18) Wang, T.; Salvatierra, R. V.; Jalilov, A. S.; Tian, J.; Tour, J. M. *ACS Nano* **2017**, *11*, 10761–10767.
- (19) Wang, T.; Zheng, Y.; Raji, A.-R. O.; Li, Y.; Sikkema, W. K. A.; Tour, J. M. *ACS Appl. Mater. Interfaces* **2016**, *8*, 14169–14173.
- (20) Raji, A.-R. O.; Varadhachary, T.; Nan, K.; Want, T.; Lin, J.; Ji, Y.; Genorio, Y.; Zhu, Y.; Kittrell, C.; Tour, J. M. *ACS Appl. Mater. Interfaces* **2016**, *8*, 3551–3556.

Materials for Bioelectronics

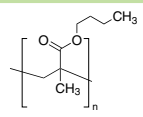
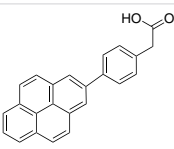
TokeOni and Analogue, Water Soluble NIR Emitters

Name	Structure	Luminescence Peak Wavelength	Cat. No.
2-[(1E,3E)-6-[3-(Dimethylamino)pyridine]-1,3-butadien-1-yl]-4,5-dihydro-4-thiazolecarboxylic acid		670-680 nm	900952-5MG 900952-25MG
2-[(1E,3E)-6-[3-(dimethylamino)pyridine]-1,3-butadien-1-yl]-4,5-dihydro-(4S)-4-thiazolecarboxylic acid sodium salt		670-680 nm	902268-1MG 902268-5MG
TokeOni		670-680 nm	808350-5MG 808350-25MG 808350-100MG

Graphene Quantum Dot

Name	Form	Description	Fluorescence Emission	Cat. No.
Carbon quantum dots	≥ 0.2% in H ₂ O, dispersion	quantum efficiency: >5%	$\lambda_{em} = 450-550$ nm	900414-10ML
Graphene quantum dots	powder	blue luminescent quantum yield ≥20%	$\lambda_{em} = 450 \pm 5$ nm	900726-50MG
	> 0.005% in H ₂ O, liquid	quantum yield >50%	-	900560-10ML
	1 mg/mL in H ₂ O, suspension	blue luminescent quantum yield >65%	$\lambda_{em} = 445$ nm	900708-50ML
	1 mg/mL in H ₂ O, suspension	aqua green luminescent quantum yield ≥17%	$\lambda_{em} = 530 \pm 10$ nm	900712-50ML
	powder	aqua green luminescent quantum yield >17%	$\lambda_{em} = 525$ nm	900713-50MG

Biolinker and Biopolymer for Nanomaterials

Name	Structure	Molecular Weight	Cat. No.
Poly(butyl methacrylate)		M_w 211,000	910716-5G 910716-250G
4-(2-Pyrenyl)phenylacetic acid		-	903175-250MG

Graphene-Based Materials

Graphene Devices

Name	Configuration	Description,	Cat. No.
Graphene FET chip	S10, Graphene FET with 30 Hall-bar devices and 6 2-probe configurations with varied channel geometry	Monolayer CVD grown Graphene based field effect transistors (FET) S10 Dirac point: 10-40 V Graphene field-effect mobility: >1000 cm ² /V·s Gate Oxide: 90nm SiO ₂ Metallization: Nickel/Aluminium 140 nm Resistivity of substrate: 1-10 Ω·cm Maximum gate-source voltage: ± 50 V Maximum temperature rating: 150 °C Maximum drain-source current density: 107 A/cm ²	GRFETS10-1EA
	S20, Graphene FET device with 2-probe Graphene FET sensors, can be gated by liquid	Monolayer CVD grown Graphene based field effect transistors (FET) S20 Dirac point: 10-40 V Graphene field-effect mobility: >1000 cm ² /V·s Gate Oxide: 90nm SiO ₂ Metallization: Nickel/Aluminium 140 nm Maximum gate-source voltage: ± 50 V Maximum temperature rating: 150 °C Maximum drain-source current density: 107 A/cm ²	GRFETS20-1EA

Biocompatible 3D Printing Inks

Name	Form	Description	Cat. No.
3D printing graphene ink	viscous liquid	0.12-0.15 Ω -cm (as 3D-printed fibers, not ink, 200-400 μ m diameter)	808156-5ML
3D Printing Graphite Ink	viscous liquid	Graphite Content: 30-40 wt% Solid content: 20-35%	901662-5ML 901662-25ML

Graphene Composites

Name	Form	Description	Cat. No.
Fe ₃ O ₄ /reduced graphene oxide nanocomposite	dispersion	10 mg/mL, Loading Density: 30%-70% (Fe ₃ O ₄ nanocrystal) by TEM Resistance: <10 ³ Ω /sq (reduced graphene oxide) dispersion in acetone	803804-5ML
Graphene nanoplatelets/ Polypropylene pellet	pellets	Elongation at Break: 72% Flexural Modulus: 1769 MPa, 75% increase compared to standard PP Flexural Strength: 42 MPa, 35.5% increase compared to standard PP Melt flow rate: \sim 7 g/10 min Notched Izod Impact Strength: 40 J/m, 185% increase compared to standard PP Tensile Modulus: 1374 MPa, 25% increase compared to standard PP Tensile Strength at Yield: 39 MPa, 8% increase compared to standard PP	906360-1KG
Mn ₃ O ₄ /reduced graphene oxide nanocomposite	dispersion	10 mg/mL in acetone, 10 mg/mL Loading Density: 30%-70% (Mn ₃ O ₄ nanocrystal) by TEM Resistance: < 10 ³ Ω /sq (reduced graphene oxide) dispersion in acetone	803812-5ML

Graphene Oxide and Reduced Graphene Oxide

Name	Form	Description	Cat. No.
Carboxylated reduced graphene oxide	powder	Dispersible, carboxylic acid group enriched, reduced graphene oxide	910406-200MG
Graphene oxide	dispersion in H ₂ O	2 mg/mL	763705-25ML 763705-100ML
	powder or flakes	sheets	763713-250MG 763713-1G
	dispersion in H ₂ O	4 mg/mL, dispersibility: polar solvents monolayer content (measured in 0.5mg/mL): >95%	777676-50ML 777676-200ML
Reduced graphene oxide	powder (black)	octadecylamine functionalized	805084-500MG
	powder	amine functionalized	805432-500MG
	powder	piperazine functionalized	805440-500MG
	powder	tetraethylene pentamine functionalized	806579-500MG
Sulfonated reduced graphene oxide	powder	sodium salt	909130-500MG

Graphene Nanoribbons

Name	Purity	Dimension	Surface Area	Cat. No.
Graphene nanoribbons, alkyl functionalized	\geq 85% carbon basis, TGA	2-15 μ m \times 40-250 nm	BET surf. area 38 m ² /g	797766-500MG
Graphene nanoribbons	\geq 90.0% carbon basis, TGA	2-15 μ m \times 40-250 nm	BET surf. area 48-58 m ² /g	797774-500MG

Carbon Nanotube Inks

SWCNT Concentration	Form	Viscosity	Description	Cat. No.
0.2 g/L (by Absorbance at 854 nm)	dispersion in H ₂ O (black liquid)	\sim 1.0 mPa.s	resistance <400 Ω /sq (by 4-point probe on prepared film by spray)	791490-25ML 791490-100ML
1.00 +/- 0.05 g/L (SWCNT concentration by Absorbance at 854 nm)	dispersion in H ₂ O (black liquid)	3.0 mPa.s (at 10 sec ⁻¹ shear rate)	sheet resistance <600 Ω /sq (at 85% VLT (ohm/square), by 4-point probe on prepared film by rod coating)	791504-25ML 791504-100ML
1 mg/mL	viscous liquid (black)	17.7 Pa.s at 25 $^{\circ}$ C (at 10 sec ⁻¹ shear rate)	sheet resistance <1000 Ω /sq (by 4-point probe on prepared, at 87.5% VLT (ohm/sq))	792462-25ML 792462-100ML
Solid content: 10 wt% solid (CNT/PLA nanocomposite) in dichloromethane (30 wt% of CNT in solid part)	viscous paste	-	Conductivity: 5050 S/m	902950-20ML
Concentration: 10 wt% solid (CNT/PLA nanocomposite) in dichloromethane (20 wt% of CNT in solid part)	viscous paste	-	Conductivity: 2111 S/m	902969-20ML
Solid content: 18 wt% solid (CNT/PLA nanocomposite) in dichloromethane (10 wt% of CNT in solid part)	viscous paste	-	Conductivity : 1389 S/m	902977-20ML

Carbon Nanotubes

Name	Assay/Carbon Content	Dimensions	Origin Of Nanomaterial	Cat. No.
Carbon nanotube array, multi-walled	98% (carbon as CNT)	H 0.5 mm diam. × L 10-40 × 0.5 ±0.1 mm	Chemical Vapor Deposition (CVD) method.	901051-1EA
	≥98% (carbon as CNT)	diam. × L 10-40 nm × 1.0 mm ±0.1 mm	Chemical Vapor Deposition (CVD) method.	901052-1EA
	>95 atom % carbon basis (x-ray)	L 100-150 nm × 30 μm (SEM)	Plasma-Enhanced Chemical Vapor Deposition (PECVD) Method	687804-1EA
Carbon nanotube array, multi-walled, drawable	98% (carbon as CNT)	L 10-40 nm × 1.0 mm ±0.5 mm	Chemical Vapor Deposition (CVD) method.	901046-1EA
Carbon nanotube, double-walled	≥90% carbon basis	L 3.5 nm × >3 μm (TEM)	Catalytic Carbon Vapor Deposition (CCVD) Method	755141-1G
Carbon nanotube, few-walled	≥94% (carbon as CNT by TGA)	D × L 2.5-3 nm × 2-6 μm	CoMoCAT™ synthesis process	900788-250MG 900788-1G
Carbon nanotube, multi-walled	>98% carbon basis	O.D. × L 6-13 nm × 2.5-20 μm	Chemical Vapor Deposition (CVD) Method	698849-1G
	>95% carbon basis	L 9.5 nm × 1.5 μm (TEM)	Catalytic Carbon Vapor Deposition (CCVD) Method	755133-5G
Carbon nanotube, multi-walled, carboxylic acid functionalized	>80% carbon basis	L 9.5 nm × 1.5 μm	Catalytic Carbon Vapor Deposition (CCVD) Method	755125-1G
Carbon nanotube sheet	>95% (carbon)	size × thickness 100 mm × 100 mm × 1-5 μm	Chemical Vapor Deposition (CVD) method.	901082-1EA
	>95% (carbon)	size × thickness 50 mm × 50 mm × 1-5 μm	Chemical Vapor Deposition (CVD) method.	901056-1EA
Carbon nanotube, single-walled	≥90% carbon basis (≥77% as carbon nanotubes)	D × L 0.83nm × 1 μm	CoMoCAT™ Catalytic Chemical Vapor Deposition (CVD) Method	704121-250MG 704121-1G
	≥95% carbon basis (≥95% as carbon nanotubes)	D × L 0.78nm × 1 μm	CoMoCAT™ Catalytic Chemical Vapor Deposition (CVD) Method	773735-250MG 773735-1G
	98% (Semiconducting) 2% (Metallic)	L 0.3-5 μm	Electric Arc Discharge Method	750522-1MG
	30% (Metallic) 70% (Semiconducting)	L 0.3-5 μm	Electric Arc Discharge Method	750514-25MG
	70% (Semiconducting) 30% (Metallic)	L 0.3-5 μm	Electric Arc Discharge Method	750492-100MG
	2% (Semiconducting) 98% (Metallic)	L 0.3-5 μm	Electric Arc Discharge Method	750530-1MG
	≥95% carbon basis (≥99% as carbon nanotubes)	Diameter 0.84nm × L 1μm	CoMoCAT™ Catalytic Chemical Vapor Deposition (CVD) Method	775533-250MG 775533-1G
	>99%, TGA (carbon content, EDX) ≥93%, TGA (carbon as SWNT by TEM)	L >5 μm (By AFM) diam. 1.2-2.0 nm (By Optical absorption)	-	901634-25G
Carbon nanotube, single-walled, amide functionalized	>90% carbon basis	D × L 4-6 nm × 0.7-1.0 μm (bundle dimensions)	Electric Arc Discharge Method	685380-100MG
Carbon nanotube, single-walled, carboxylic acid functionalized	>90% carbon basis	D × L 4-5 nm × 0.5-1.5 μm (bundle dimensions)	Electric Arc Discharge Method	652490-250MG 652490-1G
Carbon nanotube, single-walled, polyaminobenzene sulfonic acid functionalized	75-85% carbon basis	D × L 1.1 nm × 0.5-1.0 μm (bundle dimensions)	Electric Arc Discharge Method	639230-100MG
Carbon nanotube, single-walled, poly(ethylene glycol) functionalized	>80% carbon basis	D × L 4-5 nm × 0.5-0.6 μm (bundle dimensions)	Electric Arc Discharge Method	652474-100MG
Single wall carbon nanotubes	-	-	-	NIST2483 -250MG

Accelerate YOUR RESEARCH

Graphene and Carbon Nanomaterials

We strive to be the first to bring the latest graphene products to market to help accelerate your research.

- Graphene and Graphene Nanoribbons
- Graphene Nanocomposites
- Graphene Oxide and Reduced Graphene Oxide
- Carbon Nanotubes and Nanohorns
- Fullerenes

For a complete list visit:

SigmaAldrich.com/graphenotech



© 2020 Merck KGaA, Darmstadt, Germany and/or its affiliates. All Rights Reserved. MilliporeSigma, the vibrant M and Sigma-Aldrich are trademarks of Merck KGaA, Darmstadt, Germany or its affiliates. All other trademarks are the property of their respective owners. Detailed information on trademarks is available via publicly accessible resources.

The life science business of Merck KGaA, Darmstadt, Germany operates as MilliporeSigma in the U.S. and Canada.

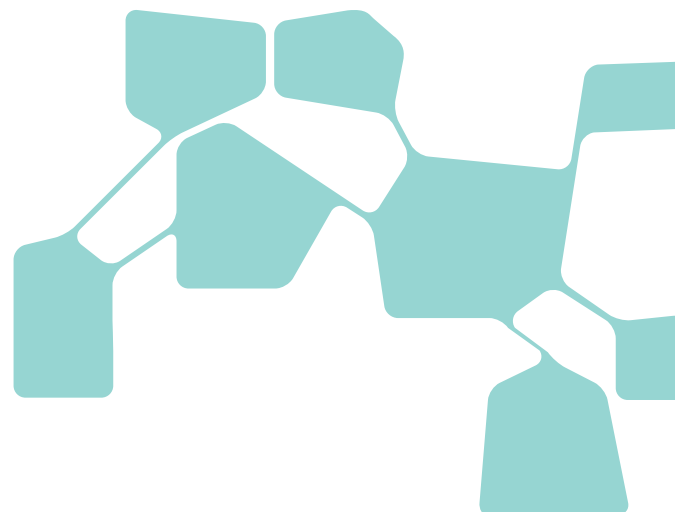
Sigma-Aldrich®
Lab & Production Materials

Recent Technology Advancements in the Fabrication of Integrated Organic Electronics



Yasunori Takeda, Shizuo Tokito

Research Center for Organic Electronics, Yamagata University, 4-3-16, Jonan, Yonezawa, Yamagata, 992-8510, Japan
Email: y.takeda@yz.yamagata-u.ac.jp, tokito@yz.yamagata-u.ac.jp



Introduction

Electronics based on organic semiconductor materials are called organic electronics. Typical applications are organic transistors, organic light-emitting diodes, and organic solar cells. Compared to conventional approaches, organic electronics are lightweight, flexible, and thinner, enabling applications such as flexible displays, large-area, lightweight solar cells, electronic skins, and the like.

Since an organic semiconductor can be processed at low temperatures, thin film layers can be formed on plastic film substrates with low heat resistance such as polyethylenenaphthalate (PEN, **Cat. Nos. GF23662043, GF58055766**). Furthermore, it is possible to fabricate electronic devices using printing techniques by creating inks that employ soluble semiconductor materials. Fabricating an electronic device using printing techniques instead of vacuum process provides for electronic devices that are scalable over large areas, drastically reducing production costs.

We will focus on organic thin-film transistors (OTFT) in this review. The performance and solubility of the organic semiconductors used in OTFTs are improving year by year. Carrier mobility is a primary semiconductor performance metric, and many materials have exhibited values of 10 cm²/Vs or more, exceeding that of amorphous silicon (a-Si) TFT devices.

Most research on OTFT devices has focused on the various aspects of organic semiconductor materials, gate insulator materials, electrode formation methods, device structures, surface treatments, and applications for integrated circuits. In this paper, we will share insights gained through the

development of the fabrication processes for OTFT devices and their integrated circuits, and report on the results gained from evaluation of their electrical characteristics.

Realization of Integrated Circuits Using Organic Thin-Film Transistors

Our research group has not only developed advanced semiconductor materials for OTFT device fabrication, but we have also extensively researched OTFT device architectures and integrated circuits and carried out new application development.

Fabricating OTFT devices using printing technologies is one way to take advantage of the benefits of organic electronic devices, and we are also optimizing and newly developing the printing processes employed. Here, the fabricating methods and electrical characteristics of OTFT-based integrated circuits are described.

High-Performance Fully Solution-Processed Organic Integrated Circuits Using a Pseudo-CMOS Circuit Configuration

P-type semiconductors generally exhibit higher performance than n-type semiconductors, in properties such as carrier mobility and atmospheric stability. The deep work function (W.F.) of commonly used gold or silver electrode materials align well with the highest occupied molecular orbital (HOMO)/lowest unoccupied molecular orbital (LUMO) level of the p-type semiconductor. Also, due to their low ionization potential, p-type semiconductors exhibit minimal deterioration due to moisture and oxygen.

On the other hand, n-type semiconductors are known to have lower atmospheric stability and carrier mobility than p-type semiconductors. Therefore, if an integrated circuit can be configured using only p-type OTFT devices, high-performance integrated circuits can generally be realized. The research described in this section is a pseudo-CMOS¹ (Complementary Metal Oxide Semiconductor) integrated circuit composed of p-type OTFT fabricated by either solution-based or printing processes.

The procedure of the OTFT fabrication process using fully solution-based or printing methods is as follows:

To form an electrode using the inkjet printing method, the surface state of the substrate on which the ink lands is important such that the wettability must be controlled by the base layer. In this case, a cross-linked PVP using melamine as a cross-linking agent was used as a base layer, upon which a gate electrode was formed.

Water-based solvent silver nanoparticle (SNP) ink (DIC, JAGLT-01) was used as the gate electrode material. Since water-based solvent ink is less susceptible to the coffee ring effect than hydrocarbon-based solvent inks, we used it for application to a gate electrode that requires high flatness in a bottom-gate bottom-contact (BGBC) structure (Figure 1B).

Next, a cross-linked PVP (Poly(4-vinylphenol)) film was used to form a gate dielectric layer by spin-coating. SNP ink (Cat. Nos.

900190, 901975, 901971) and a hydrocarbon-based solvent were used to form source and drain electrodes by inkjet printing.

Then, a hydrophobic polymer bank (AF1600X, DuPont) was formed around the source/drain electrodes by a dispenser system (Imaging Master 350PC, Musashi Engineering, Inc.) in order to define an area for semiconductor printing. Finally, an organic semiconductor ink in which pBTTT-C₁₆ (Figure 1A-left) is dissolved in *o*-dichlorobenzene (Cat. No. 240664) was printed by a dispenser system.

In this fabricating process, various treatment processes, such as sintering and annealing, are added after each step. The temperature is kept at 150 °C or lower during each step to enable fabrication on a flexible plastic substrate such as PEN.

Figure 1C shows the transistor characteristics of the fully solution/printing processed OTFT. The fabricated OTFT operated with good performance at an operating voltage of 20 V, mobility of 0.03 cm²/Vs, threshold voltage (V_{th}) of -1.2 V, and on/off current ratio of 10⁴.

We applied a pseudo-CMOS circuit configuration to construct an inverter circuit as the basis for an integrated circuit. The high-performance pseudo-CMOS inverter circuit can be configured using only p-type OTFTs. Figure 1D shows a microscopic image of the fabricated pseudo-CMOS circuit, and Figure 1E shows a circuit diagram. Figure 1F-G show the input-output and

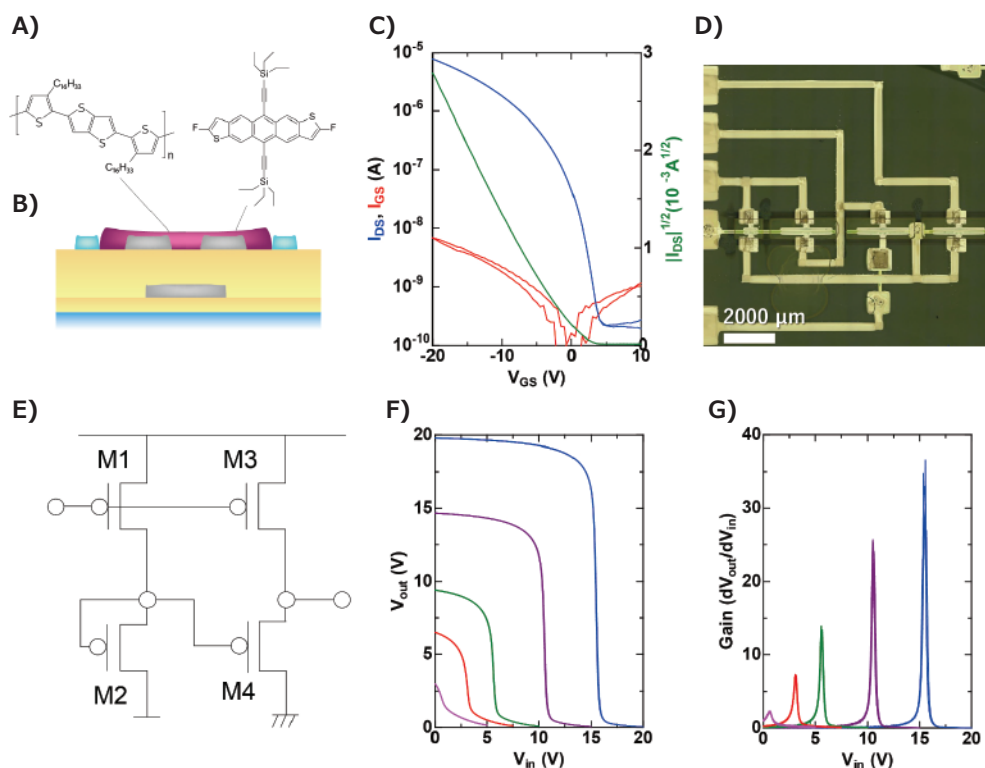


Figure 1. A) Chemical structure of the p-type organic semiconductor material. The left side shows the polymer semiconductor, pBTTT-C₁₆, and the right side shows low molecular semiconductor, diF-TES-ADT. B) Cross-sectional image of the fully printed or solution-processed organic thin-film transistor, which has a BGBC structure used in this section. C) Transfer characteristics and D) microscope image of the fabricated OTFT device. E) Circuit diagram of pseudo-CMOS circuit and F) input / output characteristics and G) gain characteristics of the fabricated pseudo-CMOS inverter circuit.

gain characteristics for a pseudo-CMOS inverter circuit using the fabricated OTFT devices. Operating began from a supply voltage of 5 V, and a gain of 34 was obtained at 20 V, excellent performance values for a fully solution-processed type inverter circuit. Using the same processes, basic gates of digital circuits such as NAND (Negative AND) and NOR (Negative OR) circuits were fabricated and also showed good performance.¹

The OTFT device performance was further improved by applying a self-assembled monolayer (SAM) surface treatment to the source/drain electrode surfaces and using a small molecule solution (diF-TES-ADT, Cat No. 754099), as shown in Figure 1A, right for the p-type semiconductor. As a result, we succeeded in fabricating a high-performance flip-flop (FF) circuit with the pseudo-CMOS configuration.²

Ultra-Low Voltage Drive Organic Integrated Circuit Using a Parylene Dielectric Layer

To improve the carrier mobility, it is necessary to optimize device fabrication conditions or to employ semiconductor materials with inherently high mobility. We further improved the performance of the OTFT device by changing the semiconductor materials, using polymer blends, and applying it to amplifier circuits.

In recent years, research reports on small molecular semiconductor materials with high mobility of 10 cm²/more, as C₈-2,7-dioctyl[1]benzothieno[3,2-b][1]benzothiophene (C₈-BTBT, Cat. No. 747092) and C₁₀-dinaphtho[2,3-b:2',3'-f]thieno[3,2-b]thiophene (C₁₀-DNTT) have increased. We fabricated an OTFT device using a small-molecule, p-type semiconductor material diethino[2'3'-d,3'd']-benzo[1,2,-b:4,-b']-dithiophene (DTBDT)-C₆ (Tosoh Corporation) that exhibits high mobility.⁴

When a polymer dielectric is mixed with a small-molecule semiconductor material, it is converted into an ink. The layers are separated during the drying process to form a good dielectric /semiconductor interface. In this case, polystyrene (PS) was selected for the polymer dielectric, and an optimized blend of concentrations was used.

The device structure of the fabricated OTFT device is shown in Figure 2A, and the transfer characteristics of the transistor are shown in Figure 2B. The device showed high performance, operated at an extremely low voltage of 2 V or less, a mobility of 1.1 cm²/Vs, a threshold voltage of -0.26 V, and a subthreshold slope (SS) value of 100 mV/dec. This very low SS value is generally realized from low-level trap states, and this study suggests that there are few trap levels at the semiconductor/polymer interface.⁵

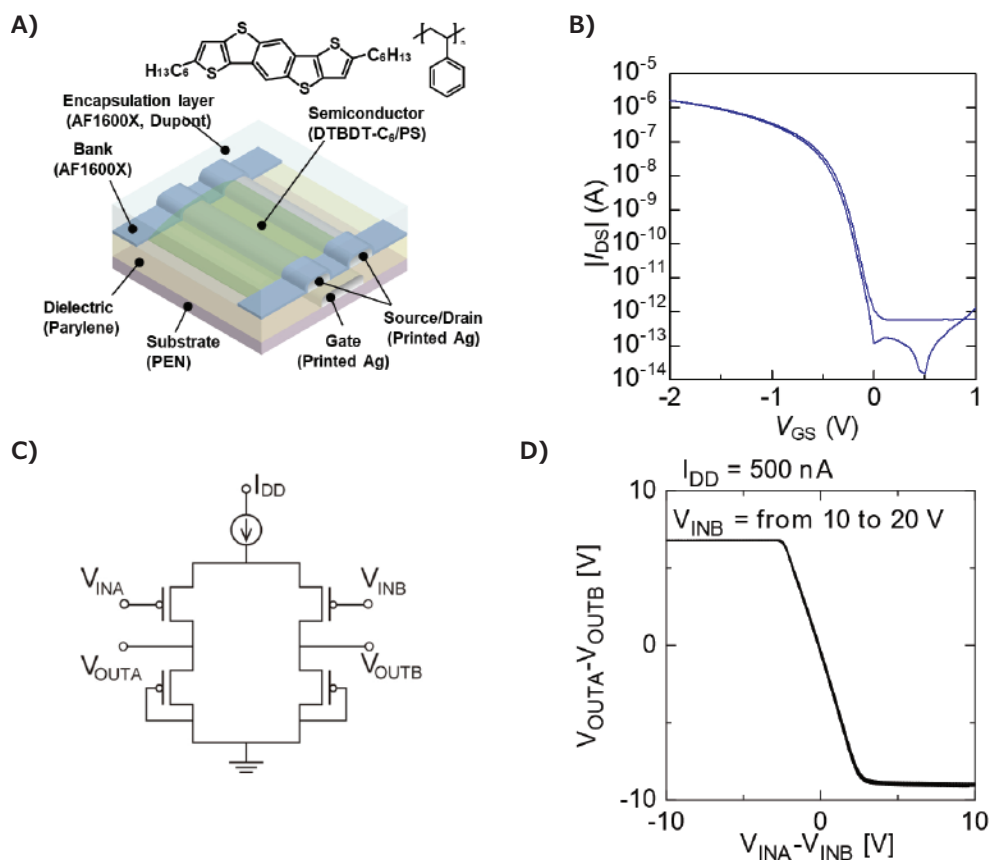


Figure 2. A). Schematic of the device structure for the fabricated low-voltage operation OTFT device and B) its transfer characteristics. C) The circuit diagram of the fabricated differential amplifier and D) its input/output characteristics.

Next, the high-performance OTFT device using DTBBDT-C₆ (dithieno[2,3-*d*;2',3'-*d'*]benzo-[1,2-*b*;4,5-*b'*]dithiophene) was used to apply to an operational amplification circuit for biosensors.⁶ DTBBDT-C₆ is known for very little variation in electrical characteristics, so a key feature of OTFT devices using DTBBDT-C₆ is small performance variations. Variations in OTFT devices cause a deviation in electrical characteristics, resulting in malfunctions when an integrated circuit is constructed. An OTFT device fabricated using DTBBDT-C₆ had an average mobility of $1.1 \pm 0.17 \text{ cm}^2/\text{Vs}$ and a threshold voltage of $-0.01 \pm 0.09 \text{ V}$, which is relatively high mobility and very small variations.

An operational amplifier circuit was fabricated using this low-variation OTFT device. The circuit diagram of the fabricated differential amplifier circuit is shown in **Figure 2C**, and typical input/output characteristics are shown in **Figure 2D**. This is a circuit that amplifies the difference between two input signals, and it is required to match the OTFT device characteristics with high accuracy. Since the fabricated organic thin-film transistors are characterized by high uniformity, a functioning operational amplifier circuit was realized.

Complementary Integrated Circuits Employing Printed OTFTs With Stacked Structures

Complementary integrated circuits require p-type and n-type OTFT devices and are expected to have higher switching performance and improved power savings than p-metal oxide-semiconductor (pMOS) and n-type metal-oxide semiconductor (nMOS) circuits using either p-type or n-type TFT devices. Therefore, a complementary integrated circuit is most suitable for electronic devices that are expected to be driven by a battery, solar cell, or bio-battery, such as wearables.

In collaboration with Ube Industries, we have developed a small molecule n-type semiconductor called TU-3 that has high atmospheric stability and high mobility (**Cat. No. 911135**). We used this n-type semiconductor to fabricate a complementary integrated circuit with a stacked structure. This approach not only improves the degree of circuit integration⁷ but also aims to form an appropriate SAM surface treatment on each of the source/drain electrodes of the p-type and n-type OTFT devices.⁸

In general, an electrode material having a deep work function is most suitable for a p-type semiconductor, and a shallow electrode material is most suitable for an n-type semiconductor. Pentafluorobenzenethiol (PFBT) has been reported as a self-assembled monolayer (SAM) surface treatment material for p-type semiconductors, and 4-Methylbenzenethiol (4-MBT, **Cat. No. T28525**) and Polyethylenimine (PEI, **Cat. No. 306185**) have been reported for n-type semiconductors.

Since immersion and spin-coating methods are generally used to form the SAM surface treatment layer, it is necessary to expose only the source/drain electrodes of the p-type/n-type OTFT or to remove the unnecessary portions after formation. Therefore, we applied a stacked structure and formed source/drain electrodes for the p-type and n-type OTFT devices in separate layers. Since the immersion method and spin-coating method are generally used as a method for forming the SAM surface treatment layer, it is necessary to expose only the source/drain electrodes of the p-type/n-type OTFT devices or to remove unnecessary portions after formation. Therefore, we employed a stacked structure and formed source/drain electrodes for the p-type and n-type OTFT devices in separate layers.

As a result, we succeeded in SAM layer formation suitable for each semiconductor using the simple immersion method. At the same time, we succeeded in increasing the degree of integration by 2 and 3 times by increasing the number of layers.⁹ **Figure 3A** shows the cross-sectional structure of the fabricated complementary integrated circuit. A photograph of the device fabricated on a 12.5 cm square glass substrate is shown in **Figure 3B**. The fabricated integrated circuit, a p-type OTFT device having a bottom-gate bottom-contact (BGBC) construction is formed on an n-type OTFT device having a top-gate bottom-contact (TGBC) construction.

The fabricated p-type and n-type OTFT devices each exhibited good performance. The p-type OTFT device using 2,8-difluoro-5,11-bis(triethylsilyl)ethynyl)anthradithiophene (diF-TES-ADT) for the semiconductor layer showed a mobility of $0.34 \text{ cm}^2/\text{Vs}$, a threshold voltage of 0.2 V, and an on/off ratio of 10^7 at an operating voltage of 10 V. The n-type OTFT device using TU-3 were $0.29 \text{ cm}^2/\text{Vs}$, 2.0 V, and 10^7 , respectively (**Figure 3C**).

Figure 3D showed the results of fabricating D-type Flip-Flop (D-FF) circuit using these OTFT devices and the evaluated circuit characteristics. The fabricated D-FF circuit worked normally and proved the feasibility of the created integrated circuits using printing processes.

Complementary Integrated Circuits Employing SAM Electrode Surface Modification For n-Type Semiconductors

A major drawback of complementary integrated circuits using stacked structures is an increase in the number of processing steps. Therefore, by using p-type semiconductors that do not require SAM surface treatment, we formed source/drain electrodes of p-type and n-type OTFT on the same plane to simplify processing. This semiconductor material employed is characterized by a wide process window that includes high-heat resistance and a variety of printing methods. When this semiconductor is used, a complementary integrated circuit can

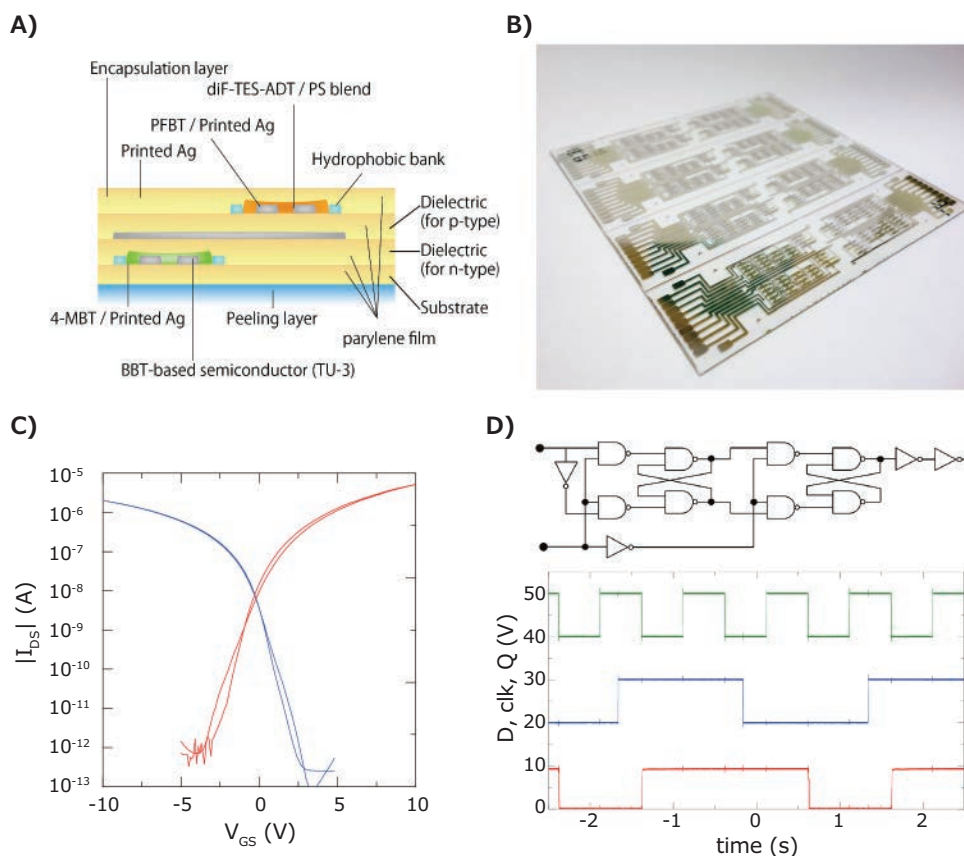


Figure 3. A). Schematic of the device structure for a complementary integrated circuit having a stacked structure and B) a photograph of devices fabricated on a 125 mm square glass substrate. C) Transfer characteristics of the fabricated p-type and n-type OTFT devices and a circuit diagram and input/output characteristics of a D-FF circuit.

be fabricated similarly to the fabricating process of a single OTFT device. First, after forming a parylene base layer on a glass substrate, SNP ink was used to form the source/drain electrode by an inkjet printing method. After that, SAM surface treatment material for n-type semiconductor is formed on all source/drain electrodes (Figure 4A).

Next, a p-type semiconductor (MOP-01, Mitsubishi Chemical) and an n-type semiconductor (TU-3, FIC) are printed using a dispenser system. Afterwards, they are annealed at 150 °C for 30 minutes. After forming the parylene as the gate insulating film, a gate electrode is formed under the same conditions as the source/drain electrodes, and a complementary integrated circuit was fabricated.¹⁰ Before forming the gate electrode, a hole was made in the gate dielectric using a YAG (Yttrium Aluminum Garnet) laser system.

The fabricated p-type and n-type OTFT devices each demonstrated good electrical characteristics. As a demonstration of the fabricated complementary integrated circuit, we formed an array of 10×10 ring oscillators on a glass substrate. The fabricated p-type and n-type organic OTFT devices had mobilities of 0.11 and 0.19 cm²/Vs, threshold voltages of 0.09 V and 1.40 V, and on/off current ratios of 10⁵ and 10⁷, respectively (Figure 4B). One-hundred (100) ring

oscillators were fabricated and were shown to operate well at a drive voltage of 1 V, and the propagation delay time per stage at 20 V was 0.34 ms (Figure 4C). The fabrication yield obtained for the ring oscillators was 100%.

Complementary Integrated Circuits Using Finely-Patterned Electrodes Formed by Reverse Offset Printing

It is difficult to miniaturize electrodes formed by the inkjet printing method, and the line width and line interval are limited. For example, electrodes formed with inkjet nozzles widely used in printed electrode research (10 pL) have electrode widths of 100 to 200 μm and line spacing (channel length: L) of 10 μm or more. Therefore, we focused on the reversal offset printing (ROP) method and succeeded in using it in forming fine electrodes.¹¹ Figure 5A shows the process step diagram for reverse offset printing. It consists of three steps: coating, patterning, and transfer. Therefore, an integrated circuit with finely patterned electrodes can be realized by combining this ROP method with a complementary integrated circuit fabricated process using a stacked structure. The manufacturing process used was the same as that used electrodes formed using the inkjet printing method.

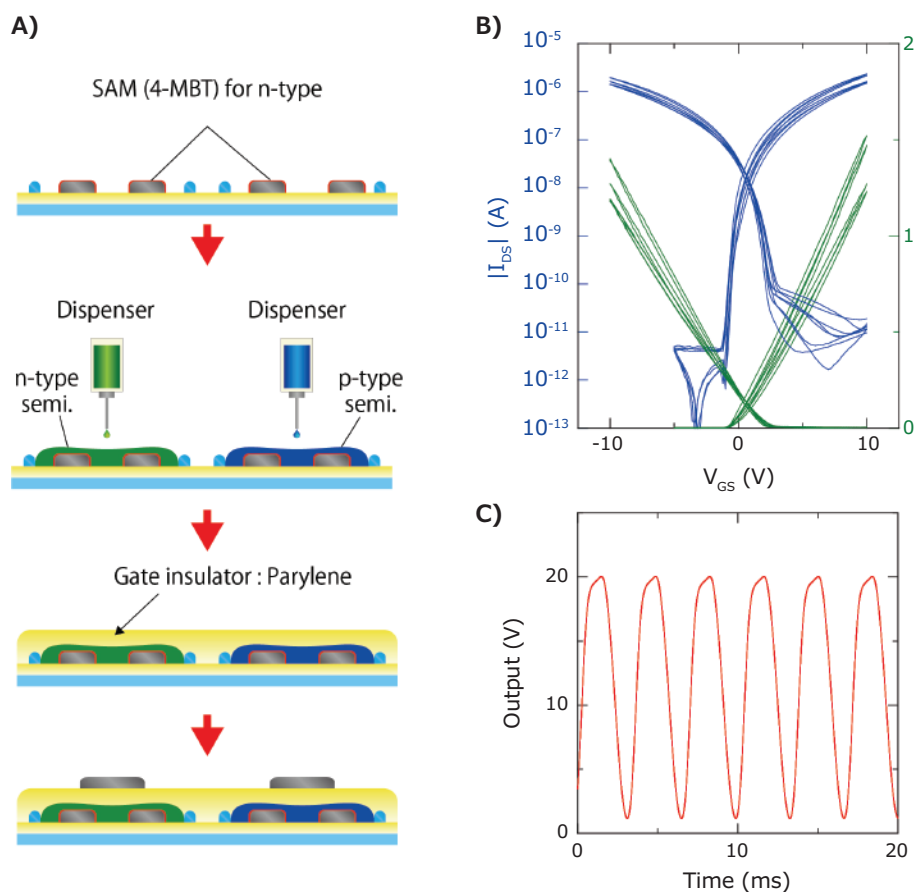


Figure 4. A) Illustration of the manufacturing process steps. B) Transfer characteristics of the fabricated OTFT device. C) Oscillation signal of the fabricated ring oscillator circuit when operating at 20 V.

The complementary integrated circuit that was formed had an electrode width of 15 μm , a line spacing of 10 μm , and a line width of about one-tenth of that of an inkjet-printed electrode. Silver nanoparticle ink (RO100GE, Future Ink Corporation) was used for electrode formation with a sintering temperature of 120 $^{\circ}\text{C}$. The variations in line spacing in the source/drain electrode patterns were less than $\pm 1 \mu\text{m}$, with a line spacing target value of 2.5 to 70 μm . **Figure 5B** shows a microscopic image of an electrode with a width of 15 μm and a line spacing of 2.5 μm . These results show that the patterning reproducibility and printing accuracy are very high. **Figure 5C** shows the input/output characteristics of the fabricated inverter circuit. Since it was found to have good electrical performance when driven from 2.5 V to 10 V,¹² it was employed to a ring oscillator circuit.

The characteristics of the fabricated ring oscillator circuit are ten times higher than that of a complementary integrated circuit fabricated by using the inkjet printing method, which is the result of a shortened-channel OTFT device and reduced overlap area.

Conclusion

We have developed fabrication processes for OTFT devices and integrated circuits using printing and solution-processing techniques. We first focused on pseudo-CMOS circuits using only p-type OTFT devices, demonstrated inverter circuits and flip-flop circuits, and evaluated the circuit operation.

In the next stage, we achieved high-mobility, low-voltage drive, and uniform characteristics using high-performance small molecule semiconductors and succeeded in fabricating ultra-low-voltage operating inverter circuits and differential amplifier circuits. We demonstrated the feasibility of amplifier circuits by employing it in biosensor signal amplification.

Finally, we developed two complementary integrated circuit fabrication processes consisting of p-type and n-type OTFT devices. One process employs a fabrication process in which the source/drain electrode layers of p-type / n-type OTFT devices are separated using a stacked structure, and the electrode surface modification is realized using a simple immersion method. The other fabrication process forms p-type and n-type

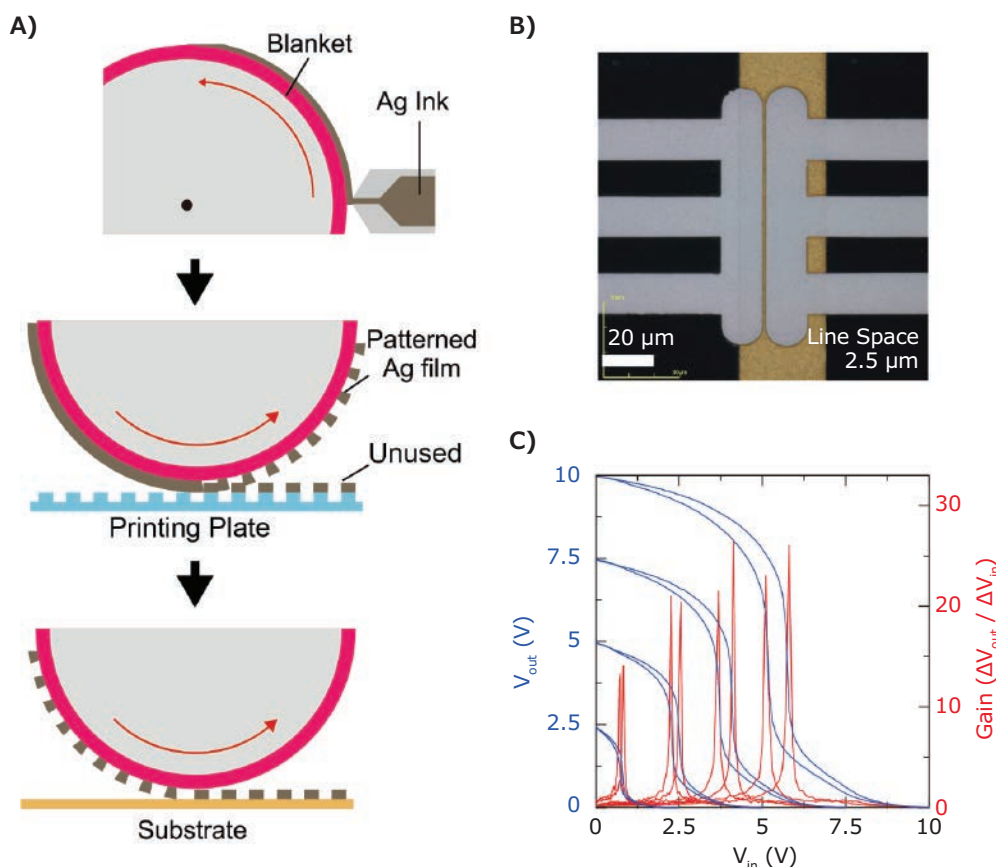


Figure 5. A) A schematic diagram of the printing steps for reverse offset printing and B) a printed silver electrode with a line width of 15 μm and a line spacing of 2.5 μm . C) Input/output characteristics of a complementary inverter circuit fabricated with finely patterned electrodes.

OTFT devices on the same plane using p-type semiconductors that exhibit high performance on various electrode surfaces. As a result, we successfully realized a complementary, integrated circuit with a small number of process steps as compared with the fabrication process using the stacked structure.

At present, many challenges remain for improving OTFT device performance and miniaturization. In the future, overcoming these issues will help to realize next-generation electronic devices such as high-performance wearable computers.

Funding Sources

JST COI Grant Number JPMJCE1312, and JSPS KAKENHI (Early-Career Scientists) Grant Numbers 18K13797.

Acknowledgments

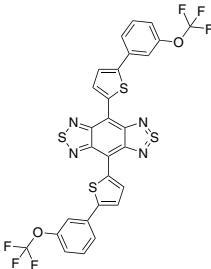
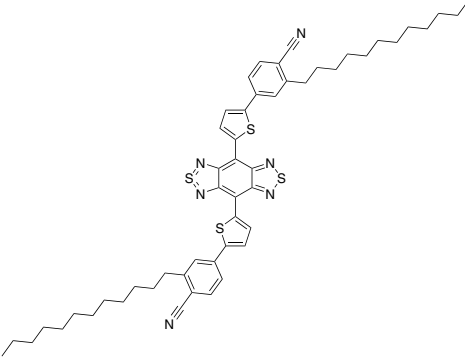
This work was partially supported by JST COI Grant Number JPMJCE1312, and JSPS KAKENHI (Early-Career Scientists) Grant Numbers 18K13797. We thank Tosoh Corporation for supplying DTBBDT-C₆ and Mitsubishi Chemical Corporation for supplying MOP-01.

Reference

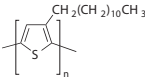
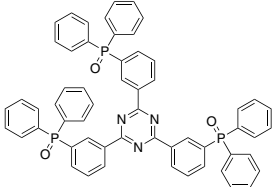
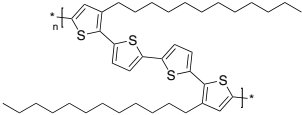
- (1) Huang, T.-C.; Fukuda, K.; Lo, C.-M.; Yeh, Y.-H.; Sekitani, T.; Someya, T.; Cheng, K.-T. *IEEE Trans. Electron. Dev.* **2011**, *25*, 141.
- (2) Takeda, Y.; Yoshimura, Y.; Kobayashi, Y.; Kumaki, D.; Fukuda, K.; Tokito, S. *Org. Electron.* **2013**, *14*, 3362.
- (3) Takeda, Y.; Yoshimura, Y.; Adib, F. A. E. B.; Kumaki, D.; Fukuda, K.; Tokito, S. *Jpn. J. Appl. Phys.* **2015**, *54*, 04DK03.
- (4) Shiwaku, R.; Takeda, Y.; Fukuda, T.; Fukuda, K.; Matsui, H.; Kumaki, D.; Tokito, S. *Sci. Rep.* **2016**, *6*, 34723.
- (5) Shiwaku, R.; Matsui, H.; Hayasaka, K.; Takeda, Y.; Fukuda, T.; Kumaki, D.; Tokito, S. *Adv. Electron. Mater.* **2017**, *3*, 1600557.
- (6) Fukuda, K.; Minamiki, T.; Minami, T.; Watanabe, M.; Fukuda, T.; Kumaki, D.; Tokito, S. *Adv. Electron. Mater.* **2015**, *1*, 1400052.
- (7) Kwon, J.; Takeda, Y.; Fukuda, K.; Cho, K.; Tokito, S.; Jung, S. *ACS Nano* **2016**, *10*, 10324.
- (8) Takeda, Y.; Hayasaka, K.; Shiwaku, R.; Yokosawa, K.; Shiba, T.; Mamada, M.; Kumaki, D.; Fukuda, K.; Tokito, S. *Sci. Rep.* **2016**, *6*, 25714.
- (9) Kwon, J.; Takeda, Y.; Shiwaku, R.; Tokito, S.; Cho, K.; Jung, S. *Nat. Commun.* **2019**, *10*, 54.
- (10) Takeda, Y.; Sekine, T.; Shiwaku, R.; Murase, T.; Matsui, H.; Kumaki, D.; Tokito, S. *Appl. Sci.* **2018**, *8*, 8980.
- (11) Fukuda, K.; Yoshimura, Y.; Okamoto, T.; Takeda, Y.; Kumaki, D.; Katayama, Y.; Tokito, S. *Adv. Electron. Mater.* **2015**, *1*, 1500145.
- (12) Takeda, Y.; Yoshimura, Y.; Shiwaku, R.; Hayasaka, K.; Sekine, T.; Okamoto, T.; Matsui, H.; Kumaki, D.; Katayama, Y.; Tokito, S. *Adv. Electron. Mater.* **2018**, *4*, 1700313.

Organic Thin-Film Transistor Materials

N-Type Semiconductors

Name	Structure	Purity/Molecular Weight	Cat. No.
TU-1		99%, HPLC	911216-50MG
TU-3		≥99%, HPLC 897.33 g/mol	911135-50MG

P-Type Semiconductors

Name	Structure	Purity/Molecular Weight	Cat. No.
Poly(3-dodecylthiophene-2,5-diyl)		99.995% trace metals basis / average $M_w \sim 27,000$	682780-250MG
PO-T2T, ≥99% (HPLC)		M_w 909.8 g/mol	907073-250MG
PQT-12		-	906921-500MG

Prefabricated Device Components for Organic Field-Effect Transistors

Name	Description	Cat. No.
Back-gated LOFET Circuit Substrate	Standard logic circuit transistors connected with inverters and ring oscillators Ti/TiN source/drain Au contact 200 nm gate-insulator, chips (diced)	FIPMS267-1PAK
Back-gated OFET Interdigitated Substrate	16 transistors per chip Au source/drain, 230 nm SiO ₂ gate-insulator varied W/L from 500 to 4000	FIPMS148-1PAK
	16 transistors per chip Au source/drain, 90 nm SiO ₂ gate-insulator varied W/L from 500 to 4000	FIPMS223-1PAK
	16 transistors per chip Au source/drain, 230 nm SiO ₂ gate-insulator varied W/L from 500 to 4000	FIPMS175-1PAK
Back-gated OFET Substrate	n-doped silicon wafer with 230 nm SiO ₂ gate-insulator	FIPMS176-1PAK
OFET Miniprober	Measuring Adaptor for Back-Gated OFET Interdigitated Substrates	FIPMS990-1EA

Conductive Inks for Printed Electronics

Screen Printing Inks

Name	Resistivity or Sheet Resistance	Viscosity At 25 °C	Cat. No.
Carbon/graphite screen printing paste fast drying	Sheet resistivity: < 50Ω/square at 25 μm (printed through 230 stainless steel mesh with 13 micron emulsion)	2.0-3.5 Pa.s (Haake RS1 C20/2° TiL at 230 sec ⁻¹ at 25 °C.)	901969-200G
Carbon/graphite screen printing paste, Coverage: 315 cm ² per g (using a 230 mesh stainless steel slow drying	Sheet resistance: < 75Ω/square at 25μm (printed through 230 stainless steel mesh with 13 micron emulsion)	3.1-5.8 Pa.s (Haake RS1 C20/2°TiL at 230 sec ⁻¹ at 25°C.)	901968-200G
Conductive silver printing ink	volume resistivity 5-6 μΩ-cm	13,000-17,000 mPa.s (at shear rate of 10 sec ⁻¹ at 25°C)	791873-10G 791873-20G
Flexible conductive silver paste for screen printing	Volume resistivity: 925 ohm cm at 60°C 527 ohm cm at 130°C	0.72-1.78 Pa.s (Haake RS1 C20/2° TiL at 230 sec ⁻¹ at 25°C)	901769-25G 901769-100G
Graphene ink, for screen printing with ethyl cellulose in terpineol, screen printable	resistivity 0.003-0.008 Ω-cm (thermally annealed 300 °C for 30 minutes, film thickness >100 nm, 25 °C)	5-50 Pa.s (shear viscosity at 10 s ⁻¹)	798983-10ML
Graphene ink in water, screen printable	sheet resistance 10 Ω/sq (at 25 μm thickness)	1800 cP (1000s ⁻¹) 350 cP (100s ⁻¹)	808261-10ML
Platinum paste, screen printable	-	2500-4500 mPa.s (Analysis carried out at 20°C with 20mm 4 degree cone/plate; 40 s ⁻¹)	791512-20G
Silver/silver chloride (60/40) paste for screen printing	Sheet resistivity:<100 miliohms per square (20 micron thick printed on alumina substrate)	2.0-5.5 Pa.s (Haake RS1 C20/2° TiL at 230 sec ⁻¹ at 25°C)	901773-50G
SunTronic® conductive silver ink for screen printing	Sheet resistivity: <0.010 Ω/sq/mil (150°C/10 min) Volume resistivity: <2.5x10 ⁻⁵ Ω.cm (150°C/30 min)	45-55 Pa.s	901879-25G

Inkjet Printing Inks

Name	Resistivity or Sheet Resistance	Viscosity	Cat. No.
Conductive nanosilver ink for inkjet printing, Silver content:18-20%W/W	-	10-18 mPa.s (25 °C, shear rate 1000 s ⁻¹)	907022-25ML
Copper inkjet ink, Cu(0) in Cu nanoparticles: >95% Particle size : d50= 50 nm; d90=120 nm (by Lumisizer™)	-	32 cP (Brookfield, Cone Spindle 40, 25°C)	907413-5ML
Graphene ink, for inkjet printing with ethyl cellulose in cyclohexanone and terpineol, inkjet printable	resistivity 0.003-0.008 Ω-cm (thermally annealed 250°C for 30 minutes, film thickness >100 nm)	8-15 mPa.s at 30 °C	793663-5ML
Graphene ink in water, inkjet printable	sheet resistance 4k Ω/sq (80 nm thickness)	1 cP (100s ⁻¹)	808288-5ML
Poly(3,4-ethylenedioxythiophene)-poly(styrenesulfonate), conductive inkjet ink	sheet resistance 110 Ω/sq	7-12 cP at 22 °C	739316-25G
SunTronic® silver nanoparticle ink for inkjet printing, Silver content: 45-50% Sintering temperature: 100 - 150°C for 10 - 60 min Solid content: 48-52% Volume Resistivity: 5 - 25 uΩcm sintering temperature 100 - 150°C	-	6-8 cP (Brookfield)	901975-2ML 901975-10ML
SunTronic® silver nanoparticle ink for inkjet printing, Sintering temperature: 150-250 °C for 10 - 60 min Solid content: 40% Volume Resistivity: 5 - 30 uΩ.cm sintering temperature: 150-250 °C	-	11-13 cP (Brookfield)	901971-2ML 901971-10ML

Flexographic Printing

Name	Resistivity or Sheet Resistance	Viscosity	Cat. No.
Graphene ink in water, flexo/gravure/screen printable	Sheet resistance 10 Ω/sq, 25μm thickness	140 cP (1000s ⁻¹) 570 cP (100s ⁻¹)	805556-10ML
SunTronic®aqueous silver flexo ink	volume resistivity: <37.5 Ω-cm	19-21 poise	901876-20G
SunTronic® conductive graphite ink for flexographic printing	Sheet resistance: < 100 Ω/sq (flexo printed on SBS board with 18 BCM anilox roll)	1300-1700 cP (Brookfield - low shear)	901970-250G

Laser-Induced Forward Transfer (LIFT) Printing

Name	Resistivity	Viscosity	Cat. No.
Conductive silver printing ink	resistivity 30 - 35 $\mu\Omega\text{-cm}$	6000-9000 mPa.s (at shear rate of 10 sec^{-1} at 25°C)	791903-10G 791903-20G
Silver ink, 75 wt%, LIFT printable	After laser sintering $\leq 8 \mu\Omega\text{-cm}$ (≤ 5 bulk) for LIFT printed line ($\sim 1\text{-}2 \mu\text{m}$ thick) on plastic substrate	50,000-100,000 cP (Shear Rate: 1 s^{-1}) 250cP - 450 cP (Shear Rate: 1000 s^{-1})	907669-5G

3D Printing

Name	Resistivity	Viscosity At 20 °C (Pa.s)	Cat. No.
3D printing graphene ink, 0.12-0.15 $\Omega\text{-cm}$ (as 3D-printed fibers, not ink, 200-400 μm diameter)	0.12-0.15 $\Omega\text{-cm}$ (3D printing by direct extrusion into 200-400 μm diameter)	25-45 (At low shear stresses. Shear thins to $\sim 10\text{-}15$ Pa.s at Shear Stress = 100 Pa)	808156-5ML
3D printing graphene ink, Graphite Content: 30-40 wt% Solid content: 20-35%	-	20-60	901662-5ML 901662-25ML

Gravure Printing

Name	Resistivity	Viscosity At 25 °C (Pa.s)	Cat. No.
Graphene ink, for gravure printing with ethyl cellulose in terpineol, gravure printable	0.003-0.008 $\Omega\text{-cm}$ (thermally annealed 250 °C for 30 minutes, film thickness >100 nm)	0.75-3 (shear viscosity at 100 s^{-1} , 25 °C)	796115-10ML

Dielectric Inks for Printed Electronics

Inkjet Printing Ink

Name	Viscosity (cP)	Cat. No.
SunTronic® UV curing jettable insulator for low-K dielectric applications	11-13 (at jetting temperature)	901974-250ML

Screen Printing Inks

Name	Viscosity	Cat. No.
Polymer dielectric blue for screen printing	5.5-8.0 Pa.s (Haake RS1 C20/2° TiL at 230 sec^{-1} at 25 °C)	902365-250G
Polymer dielectric grey for screen printing	12.0-16.0 Pa.s (Haake RS1 C20/2° TiL at 230 sec^{-1} at 25 °C)	902497-250G
SunTronic® UV curing dielectric green for screen printing	20-30 poise (Brookfield CAP @25 °C)	901973-250G

Interfacial Inks for Printed Electronics

Slot Die, Doctor Blade, or Spin Coating

Name	Viscosity	Cat. No.
Aluminum-doped zinc oxide ink for spin coating/slot-die coating work function 3.6	<4 mPa.s at 20 °C	901092-25ML
Aluminum-doped zinc oxide nanoparticle ink, 2.5 wt. % work function $\sim 4.3\text{eV}$	1.9-3.1 cP	807729-10ML 807729-50ML
Aluminum-doped zinc oxide nanoparticle ink, 2.5 wt. %, work function ~ 3.9 eV	1.7-2.7 cP	808237-10ML 808237-50ML
Molybdenum oxide nanoparticle ink	1-3 cP	900151-10ML
Plexcore® OC AQ-1250 Organic Conductive Ink	3.3-5.5 cP at 25 °C	805793-20ML
Tungsten oxide ($\text{WO}_{3,x}$) nanoparticle ink	-	793353-5ML 793353-25ML 793353-50ML
Zinc oxide ink for spin coating/slot-die coating work function 4.0	<4 mPa.s at 20 °C	901081-25ML
Zinc oxide nanoparticle ink	-	793361-5ML 793361-25ML 793361-50ML
Zinc oxide nanoparticle ink work function $\sim 3.9\text{eV}$	1.6-2.6 cP	808253-10ML 808253-50ML

Inkjet Printing

Name	Viscosity At 20 °C	Cat. No.
Aluminum-doped zinc oxide ink for inkjet printing work function 3.6	10 mPa.s ±3 mPa.s	901065-25ML
Aluminum-doped zinc oxide nanoparticle ink, 2.5 wt. % work function -4.3eV	2.4-4.0 cP	807656-10ML 807656-50ML
Aluminum-doped zinc oxide nanoparticle ink, 2.5 wt. % work function -3.9eV	2.5-3.7 cP	808164-10ML 808164-50ML
Aluminum-doped zinc oxide nanoparticle ink, 2.5 wt. % work function -4.3eV	8-14 cP	808172-5ML 808172-10ML 808172-50ML
Aluminum-doped zinc oxide nanoparticle ink, 2.5 wt. % work function -3.9eV	8-14 cP	808180-5ML 808180-10ML 808180-50ML
Tungsten oxide nanoparticle ink, 2.5 wt% in 2-propanol and propylene glycol	8 cP	807753-5ML 807753-25ML 807753-50ML
Zinc oxide nanoparticle ink, 2.5 wt. % work function -4.3eV	8-14 cP	807613-5ML 807613-10ML 807613-50ML
Zinc oxide nanoparticle ink, 2.5 wt. % work function -4.3eV	2.4-3.8 cP	807648-10ML 807648-50ML
Zinc oxide nanoparticle ink, 2.5 wt. % work function -3.9eV	2.4-3.7 cP	808199-10ML 808199-50ML
Zinc oxide nanoparticle ink, 2.5 wt. % work function -3.9eV	8-14 cP	808202-5ML 808202-10ML 808202-50ML

Screen Printing

Name	Viscosity At 20 °C	Cat. No.
Aluminum-doped zinc oxide nanoparticle ink, 2.5 wt. % work function -4.3eV	25-37 cP	808210-10ML 808210-50ML
Aluminum-doped zinc oxide nanoparticle ink, 2.5 wt. % work function -3.9eV	32-48 cP	808229-10ML 808229-50ML
Titania paste, active opaque	40000-55000 mPa.s (Analysis carried out with 20mm 4 degree cone/plate; 40 s-1))	791555-5G 791555-20G
Titania paste, reflector	15000-25000 mPa.s (Analysis carried out with 20mm 4 degree cone/plate; 40 s-1))	791539-5G 791539-20G
Titania paste, transparent	40000-55000 mPa.s (Analysis carried out at 20°C with 20mm 4 degree cone/plate; 40 s-1))	791547-10G 791547-20G
Zinc oxide nanoparticle ink, 2.5 wt. % work function -4.3eV	26-36 cP	807621-10ML 807621-50ML
Zinc oxide nanoparticle ink, 2.5 wt. % work function -3.9eV	32-48 cP	808075-10ML 808075-50ML

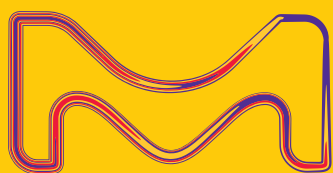
catch the SUN

Product Category list:

- Organic Photovoltaic (OPV) Donors and Acceptors
- Dye-Sensitized Solar Cell Materials
- Perovskite Materials

Visit us at:

SigmaAldrich.com/organic-electronics



© 2020 Merck KGaA, Darmstadt, Germany and/or its affiliates. All Rights Reserved. MilliporeSigma, the vibrant M and Sigma-Aldrich are trademarks of Merck KGaA, Darmstadt, Germany or its affiliates. All other trademarks are the property of their respective owners. Detailed information on trademarks is available via publicly accessible resources.

The life science business of Merck KGaA, Darmstadt, Germany operates as MilliporeSigma in the U.S. and Canada.

Sigma-Aldrich®
Lab & Production Materials

Recent Progress for High Performance Tandem Organic Solar Cells



Lingxian Meng, Xiangjian Wan, Yongsheng Chen*

The Centre of Nanoscale Science and Technology and Key Laboratory of Functional Polymer Materials, Institute of Polymer Chemistry, College of Chemistry, Nankai University, Tianjin 300071, China
State Key Laboratory of Elemento-Organic Chemistry, Nankai University, Tianjin, 300071, China
Renewable Energy Conversion and Storage Center (RECAST), Nankai University, Tianjin 300071, China
E-mail: yschen99@nankai.edu.cn

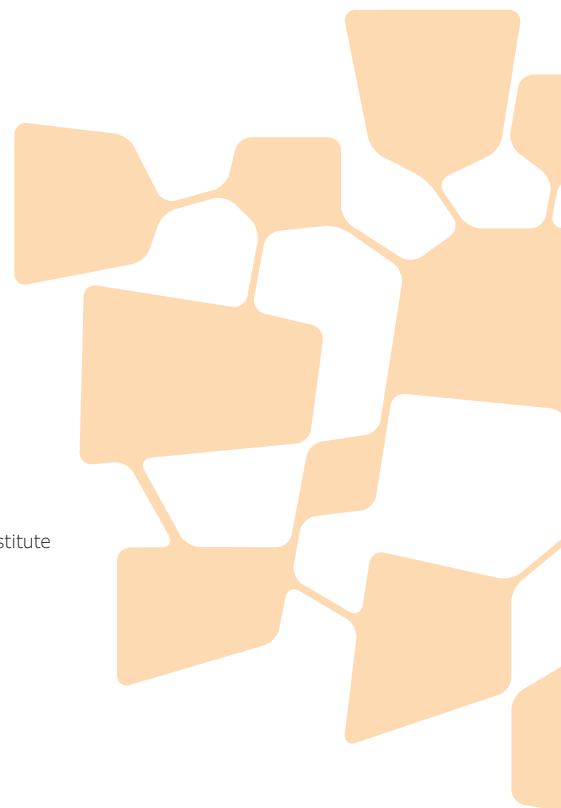
Introduction

Organic solar cells (OSCs) are widely considered one of the most promising photovoltaic technologies because they are low-cost, lightweight, flexible, and compatible with large-area-printing technologies.¹⁻³ Substantial progress has been made in the development of OSCs in the past decade. In particular, power conversion efficiencies (PCEs) have reached over 16% for single-junction OSCs through innovative material design and device optimization.⁴⁻⁶ However, despite the successes achieved by single-junction OSCs, their performance still lags far behind that of other technologies that are based mainly on inorganic materials, and their further improvement is subject to various limitations.^{1,3} First, the intrinsic, low-charge mobilities of organic materials restrict the thickness of the active layer and hinder sufficient absorption, which is detrimental for obtaining high photocurrent. Second, although the development of novel, narrow-band gap polymers and small molecule materials has widened the absorption spectrum range of the active layer of OSCs, the inherent narrow absorption windows of organic semiconductors still limits the photocurrent.^{3,7} In addition, single-junction OSCs inevitably suffer from the serious thermalization loss of photon energy.⁸

One effective way to address these issues is to develop tandem devices with two or more sub-cells and complementary absorption spectra connected together. This approach can not only overcome the fundamental limits already outlined, more importantly, it makes full use of the advantages of organic

materials, their diversity, easily tunable band structure, and facile synthesis.^{1,3} Furthermore, tandem devices maximize the absorption of OSCs and simultaneously reduce thermalization losses, significantly improving the PCEs of the devices.⁸⁻⁹

The most effective and widely studied tandem devices are the series-connected double-junction type, in which active layers are stacked in series through interconnection layers (ICLs).⁸ The front sub-cell based on wide bandgap materials absorbs light of shorter wavelength, and the rear sub-cell based on narrow bandgap materials make use of longer wavelength light. The complementary absorption of the two sub-cells maximizes the use of sunlight and further improves the performance of the device.⁸ Besides absorption spectra, there are many other factors that need to be considered in order to pursue higher PCEs for the series-connected tandem devices. First, on the basis of complementary absorptions, the two sub-cells should also possess well-balanced and high, short-circuit currents (J_{sc}) since the J_{sc} of tandem solar cells is limited by the sub-cells with smaller J_{sc} . Second, in series-connected tandem solar cells, the open-circuit voltage (V_{oc}) is expected to be the sum of the sub- V_{oc} s. The two sub-cells should have minimal energy loss to retain higher sub- V_{oc} s. Third, the ICLs should be highly transparent and robust enough to protect underlying layers, and they should form ohmic contact with subcell active layers to ensure efficient charge extractions.^{3,8}



Many explorations have been made for organic tandem cells in the past decade, and photovoltaic performance has recently reached 17%.¹⁰ In this review, the recent progress of tandem OSCs, especially that of non-fullerene (NF) systems, will be discussed. Subsequently, the efficiency prediction for tandem OSCs will be discussed through a semi-empirical analysis model reported earlier, which could provide guidance for material selection in each sub-cell to achieve high efficiency for tandem cells. Last, a general summary and outlook will be discussed at the end of the review.

State-of-the-Art Tandem Organic Solar Cells

Most of the tandem OSCs reported in earlier literature are based on polymer/small-molecule donor materials and fullerene acceptors, in which PCEs of 11.6% and 12.7% have been achieved for polymer donors and small molecule-based tandem devices, respectively.¹¹⁻¹² Devices based on fullerene derivatives are expected to obtain a well-balanced J_{sc} through the appropriate selection of donor materials with different band gaps, since fullerene derivatives contribute little to the absorption of the blend films. However, the intrinsic narrow absorption bands of organic semiconductors do not cover a broad-enough range of the solar spectrum and thus lead to a low and unbalanced photocurrent.¹³ Furthermore, fullerene derivative-based, single-junction OSCs generally have high voltage loss, which limits the V_{oc} of tandem devices.¹³ Recently, organic solar cells based on non-fullerene acceptors have made substantial progress and attracted significant attention. Compared with fullerene derivatives, non-fullerene acceptor materials, show many advantages, including 1) more efficient structure tunability (and thus higher bandgap adjustability) making it easier for these materials to complement the absorption of the donors and obtain a higher photocurrent, especially in the near-infrared region; 2) lower voltage loss, which allows a higher V_{oc} in the tandem devices.¹⁻³

Among various non-fullerene acceptors, molecules with Acceptor-Donor-Acceptor (A-D-A) architecture have achieved significant success. To date, most high efficiency OPV devices using non-fullerene acceptors with PCE over 10% are fabricated using A-D-A acceptors.^{1-3,14,15} In fact, A-D-A acceptors have been developed from donor molecules with A-D-A structures.

As shown in **Figure 1**, A-D-A molecules including donor and acceptor molecules have a symmetric structure with two electron withdrawing units on the outside. This unique chemical structure is expected to contribute to significantly improved photovoltaic performance of A-D-A molecules compared to other types of molecules, such as those with D-A-D structures. This is because the interaction between donor and acceptor materials in the bulk heterojunction (BHJ) devices plays an important role in the photovoltaic process, where the interaction mainly depends

on the lowest unoccupied molecular orbital (LUMO) of the donor and acceptor after photo-induced excitation and generation of exciton. Proper interaction between two such LUMO orbitals is expected to favor an efficient charge separation. The outside LUMOs with all inside highest occupied molecular orbital (HOMO) for A-D-A molecules facilitate the exciton dissociation and charge separation process because of the easily formed exciton dissociation coupling with LUMOs of other donors or acceptors. This is one of the reasons that A-D-A molecules show excellent performance compared to other types of molecules. With these advantages, the tandem OSCs with A-D-A acceptor molecules have received much interest and achieved great progress in recent years.

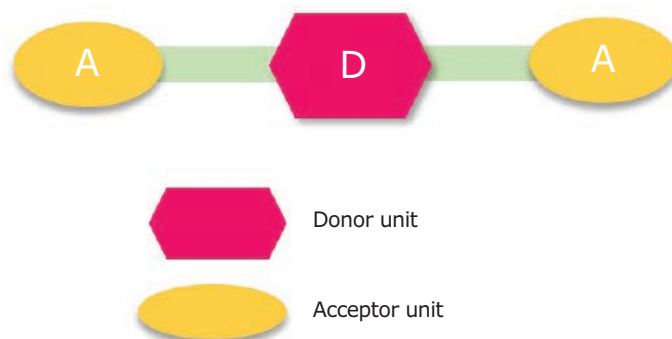


Figure 1. Schematic of A-D-A structure.

In 2016, Chen et al. reported a tandem solar cell with a high V_{oc} of 1.97 V. As shown in **Figure 2**, two acceptors, SF(DPPB)₄ and IEIC were used in the front and rear sub-cells, respectively. Meanwhile, MoO₃/ultrathin Ag/PFN was used as a dual-functional ICL. Finally, the tandem device achieved a PCE of 8.48%, which is limited by the low J_{sc} due to the much overlapped absorptions of the two subcells. With the high V_{oc} , the above tandem device has been used for solar-cell-driven water splitting tests, demonstrating the great potential of high-voltage tandem cells.¹⁶ In 2017, Yan et al. reported a homo-tandem OSC based on an all-solution processed recombination layer with a mild, thermal-annealing treatment. They used the residue moisture in PEDOT:PSS (Cat. Nos. **900181**, **655201**, **739332**), to facilitate the hydrolysis of diethyl zinc precursor and then obtained the PEDOT:PSS/ZnO recombination layer. The mutually beneficial interaction enables the recombination layer to work efficiently with a mild thermal annealing. With this, the tandem device showed a PCE of 10.8% with a high V_{oc} over 2.1 V.¹⁷

The innovation of efficient and low bandgap A-D-A type small molecule acceptors has created a great opportunity to fabricate higher efficiency tandem devices.³ The near-infrared absorption of these low band gap materials help to increase the J_{sc} of the

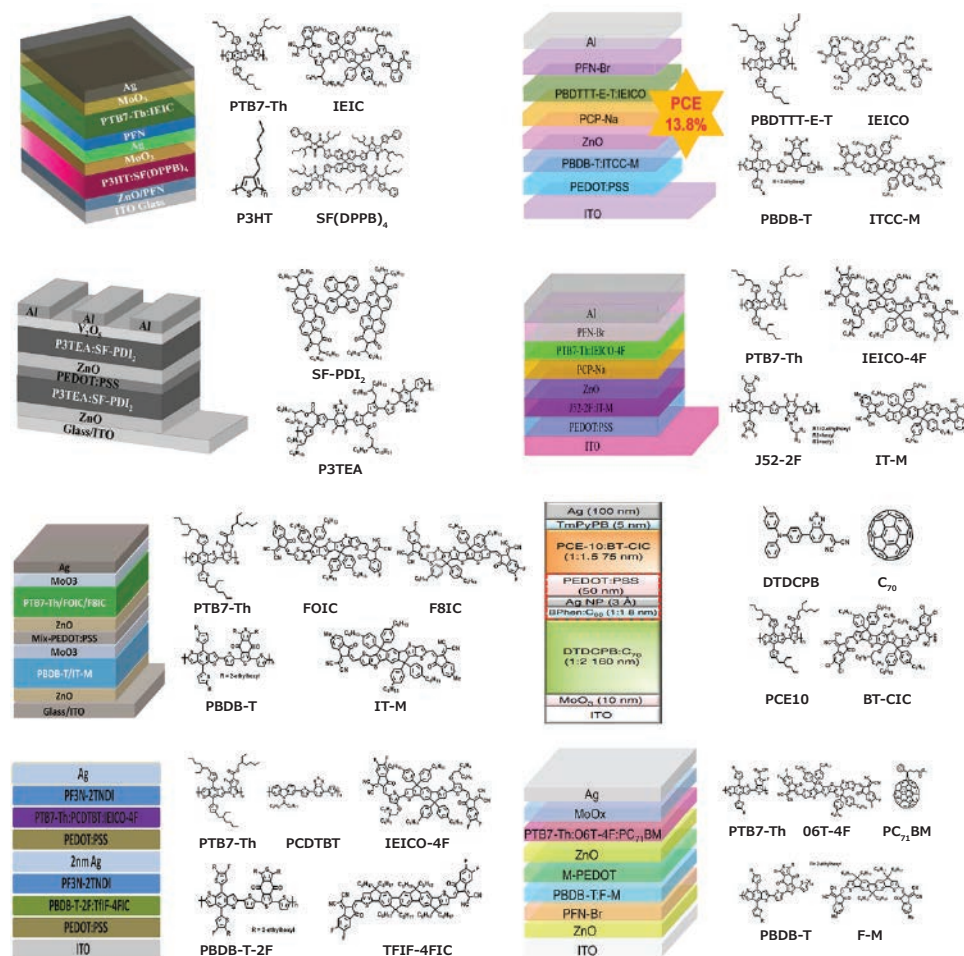


Figure 2. The tandem devices and chemical structures of the typical NF tandem solar cells. Reproduced with permission from references 10, 16-7, and 19-23, copyright and publisher listed at the end of this article.

tandem devices. In 2017, Alex et al. designed and synthesized a low-band gap electron acceptor, 4TIC, with absorption edge to ~ 900 nm. The single junction device with PTB7-Th (Cat. No. **794333**) as the donor material gave a PCE of 10.43% with J_{sc} of 18.75 mA/cm², a fill factor (FF) of 0.72 and V_{oc} of 0.78V. The high efficiency together with its small voltage loss makes PTB7-Th:4TIC a suitable rear sub-cell for tandem solar cells. The authors fabricated a series of connection tandem solar cells incorporating this rear cell and PBDB-T:ITIC (Cat. Nos. **901099**, **900799**) as the front cell, and obtained an exceptional device performance of 12.62%.¹⁸ In the same year, Hou et al. reported a tandem device with an outstanding PCE of 13.8% with a V_{oc} of 1.79 V, J_{sc} of 12.0 mA cm⁻² and FF of 0.641. They designed a new NF A-D-A acceptor ITCC-M (Cat. No. **900947**) by replacing the phenyl rings in the end groups with α -methylthiophene groups. When blended with PBDB-T as the donor material, ITCC-M based devices showed a high V_{oc} over 1 V, which is suitable as the front cell. Then, they selected the near-infrared absorption material, IEICO, as the acceptor and the low band gap donor material PBDTTT-E-T as the donor for the rear cell. A bilayer structure of ZnO/PCP-Na was used as the ICL.¹⁹ In their subsequent work,

using the same ICL and device structure, Hou et al. fabricated a tandem OSC with a high PCE of 14.9%, in which J52-2F:IT-M and PTB7-Th:IEICO-4F were used as the front and rear cell, respectively. The complementary absorption of the subcells contributed to the improved J_{sc} and enhanced PCE.²⁰

Recently, Forrest et al. demonstrated a tandem solar cell using a near-infrared A-D-A NF acceptor in the rear cell (PCE10:BT-CIC) and an evaporated small molecule in the front cell (DTDCPB). With an antireflection coating on the back of the glass substrate, a PCE of 15% was obtained. The large area device (1 cm²) showed a PCE of over 11.5%.²¹ Yang et al. employed a ternary non-fullerene system in rear sub-cell (PTB7-Th/FOIC/F8IC) to balance the voltage-current trade-off in tandem OSCs. A PCE of 13.3% was achieved.²² Huang et al. fabricated a tandem device using an NFA TfIF-4FIC (with a core of fused non-acyclic unit and end capping groups of 2-(5,6-difluoro-3-oxo-2,3-dihydro-1H-inden-1-ylidene)malononitrile) in the front cell and the low-bandgap acceptor IEICO-4F in the rear cell. After device optimization, a high PCE of 15% was obtained.²³

Based on the series of A-D-A molecules we developed, researchers in our group started to study tandem devices five year ago. At first, we fabricated a series of tandem devices using A-D-A molecules as donors and fullerene derivatives as acceptors. An outstanding PCE of 12.7% was achieved in 2017, which was the best value for fullerene based devices at that time.¹² In subsequent work, we designed two new A-D-A small molecule acceptors named F-M (**Cat. No. 906972**) and NOBDT with an absorption range from 300 to 900 nm. Using PBDB-T:F-M as the front sub-cell and PTB7-Th:NOBDT as the rear sub-cell, a conventional tandem device was fabricated with an outstanding PCE of 14.11%.²⁴ Later, using two subcells with the same donor PBDB-T and two acceptors F-M and NNBDT with complementary absorptions to balance the V_{oc} and J_{sc} , we fabricated an efficient inverted tandem OSC with an optimized PCE of 14.52%, a high V_{oc} of 1.82 V, a notable FF of 74.7% and a J_{sc} of 10.68 mA cm⁻².²⁵

While the development of NF tandem OSCs has led to much progress in PCE, the resulting J_{sc} s were still unsatisfactory, limiting tandem device efficiency. As a result, broadening the absorption range of the NF materials became a focus for generating further improvement of the J_{sc} of tandem devices. With the guidance of semi-empirical analysis (discussed in detail in the following section), we developed and reported on a tandem device that uses two A-D-A acceptor based subcells with complementary absorptions. PBDB-T: F-M was selected as the front cell because of its high voltage and suitable absorption range from 300-750 nm. A low band gap A-D-A small molecule acceptor, O6T-4F (**Cat. No. 906379**), was used in the rear cell since the rear cell PTB7-Th: O6T-4F:PC₇₁BM has absorption up to 1050 nm and higher J_{sc} — approximately matching the absorptions with the front cell. After device optimization, a record PCE of 17.36% was achieved, which is the highest value

for tandem devices to date.¹⁰ The aforementioned photovoltaic parameters of NF tandem devices are summarized in **Table 1**.

Efficiency Prediction for Organic Tandem Solar Cells

Previous efficiency predictions of tandem OSCs are mostly based on the use of fullerene acceptors.⁸ Since NF tandem OSCs have yielded better results as previously mentioned, the predictions based on NF tandem devices would clearly benefit from re-evaluation using these improved factors. In 2018, we proposed a semi-empirical model to direct the selection of materials for each sub-cell with optimized tandem cell efficiency. With the guidance of this semi-empirical analysis, a remarkable new record PCE of 17.36% has been achieved.¹⁰ The following is the main content of this model:

The semi-empirical analysis was based on a 2-terminal monolithic tandem cell with two subcells in series.¹⁰ Based on the equation of $PCE = J_{sc} \times V_{oc} \times FF / P_{in}$ (P_{in} is the power density of the incident light), to achieve a best PCE under AM 1.5G, the J_{sc} , V_{oc} and FF need to be maximized simultaneously. Thus, firstly, the sub-cells need to have ideal J_{sc} in the corresponding absorption range and maximized V_{oc} (meaning minimized E_{loss}). Also, there is a trade-off between the maximized J_{sc} and V_{oc} as the multiplication of these two factors decide the eventual PCEs.¹⁰ The two photovoltaic parameters J_{sc} and V_{oc} of a 2-terminal monolithic tandem cell are obtained as follows:

$$(1) \quad J_{sc,tandem} = \frac{1}{2} \cdot \int_{300}^{\lambda_1} \frac{q\lambda}{hc} \cdot E(\lambda) \cdot EQE(\lambda) d\lambda = \int_{300}^{\lambda_2} \frac{q\lambda}{hc} \cdot E(\lambda) \cdot EQE(\lambda) d\lambda$$

$$(2) \quad V_{oc,tandem} = V_{oc,front} + V_{oc,rear} = \frac{1}{q} \left(\frac{1240}{\lambda_2} + \frac{1240}{\lambda_1} - 2E_{loss} \right)$$

Table 1. Photovoltaic performance of NF tandem organic solar cells covered by the references.

Front subcell			Back subcell			Tandem				Ref.	
Material	Eg (eV)	Voc (V)	Material	Eg (eV)	Voc (V)	Voc (V)	Jsc (mA cm ²)	FF (%)	PCE (%)		
									Average	Best	
P3HT:SF(DPPB)4	1.80	1.11	PCE10:IEIC	1.55	0.95	1.97	8.28	52	8.21	8.48	16
P3TEA:SF-PDI2	1.72	1.11	P3TEA:SF-PDI2	1.72	1.11	2.13	8.32	60.9	/	10.8	17
PBDB-T:ITIC	1.59	0.92	PCE10:4TIC	1.40	0.77	1.65	10.62	71	12.62	/	18
PBDB-T:ITCC-M	1.70	1.00	PBDTTT-E-T:IEICO	1.34	0.92	1.8	12.0	63.9	13.1	13.8	19
J52-2F:IT-M	1.60	0.95	PCE10:IEICO-4F	1.24	0.71	1.65	13.3	68.0	14.5	14.9	20
DTDCPB:C70	1.68	0.90	PCE10:BT-CIC	1.38	0.69	1.59	13.3	71.0	/	15.0	21
PBDB-T:IT-M	1.61	0.91	PCE10:FOIC:F8IC	1.31	0.72	1.62	10.6	73.9	12.7	13.3	22
PBDB-T-2F:TFIF-4FIC	1.60	0.98	PCE10:PCDTBT:IEICO-4F	1.24	0.69	1.6	13.6	69	14.8	15	23
PBDB-T:F-M	1.65	0.98	PCE10:NOBDT	1.39	0.77	1.71	11.72	70	13.92	14.11	24
PBDB-T:F-M	1.65	0.99	PBDB-T:NNBDT	1.38	0.86	1.82	10.68	74.7	14.03	14.52	25
PBDB-T:F-M	1.65	0.94	PCE10:O6T-4F:PC70BM	1.20	0.69	1.64	14.32	72.1	16.89	17.32	10

where $E(\lambda)$ is the spectral irradiance in AM 1.5G, λ_1 and λ_2 are the absorption onsets of the rear and the front cells, h is Planck's constant, c is the speed of light and q is the elementary charge. For tandem OSCs, the predicted PCEs should be obtained when the rear cell's absorption is up to a certain range with fixed EQE, E_{loss} and FF . Then, the requirements for the front cell materials can be selected based on the modelling results and **equation (1)**.¹⁰

Based on above assumptions, with fixed E_{loss} and FF of each sub-cell, we obtained the PCEs versus EQE and $\lambda_{\text{onset, rear cell}}$. Meanwhile, with fixed EQE and FF , the graphs of PCEs versus E_{loss} and $\lambda_{\text{onset, rear cell}}$ were obtained.¹⁰ As shown in **Figure 3B**, if the $\lambda_{\text{onset, rear cell}}$ is up to 1100 nm with an average EQE of 75%, FF being 0.75 and a typical E_{loss} of 0.6 eV, a PCE of $\sim 20\%$ can be reached. Moreover, the E_{loss} seems to make a bigger impact on the overall PCEs as shown in **Figure 3C** and **Figure 3D**. As shown in **Figure 3C**, with the fixed FF of 0.75 and EQE of 75%, when E_{loss} equals to 0.5 eV, the PCE_{max} of $\sim 22.6\%$ was obtained when the $\lambda_{\text{onset, rear cell}} = 1060\text{--}1125$ nm; when the E_{loss} is 0.6 eV, a 20.2% PCE_{max} was obtained for $\lambda_{\text{onset, rear cell}} = 1030\text{--}1100$ nm; however, when the E_{loss} is as large as 0.7 eV, the PCE_{max} of 17.8% was obtained at a large range for $\lambda_{\text{onset, rear cell}} = 900\text{--}1100$ nm. With the increase of $\lambda_{\text{onset, rear cell}}$, the PCE_{max} gradually decreases. Also, with the increase of E_{loss} , the PCE_{max} will be obtained in

a blue-shifted $\lambda_{\text{onset, rear cell}}$. Based on these results, there are several general rules that can be derived to achieve high-performance tandem devices. That is, sub-cells should have high EQE response, small E_{loss} and high FF , and the absorption of them should be complementary and sufficiently broad.¹⁰

Summary and Outlook

In this review, we discussed the rapid development of non-fullerene acceptor tandem OSCs and methods for their further improvement. Herein, based on the results from the model analysis we have presented, one should pay particular attention to these specific rules to achieve higher PCEs: 1) The rear cell should have efficient absorption in longer wavelengths and the absorption edge should be in the range of 1050–1100 nm. 2) After the materials for the rear sub-cell are selected, the materials for the front cell should be selected based on the rule that the J_{sc} of each sub-cell must be the same for the optimal tandem cell. For example, if an E_g of ~ 1.18 eV (~ 1050 nm) for rear sub-cell is selected, the front cell material should have an E_g of ~ 1.72 eV (~ 720 nm) and a wide, efficient absorption in the range from 300 to 720 nm. 3) Careful attention should be paid to the E_{loss} . In addition to the rules 1) and 2) above, we recommend using materials with smaller E_{loss} to obtain higher V_{oc} . 4) Prioritize the use of materials with higher FF , EQE, and mobility.

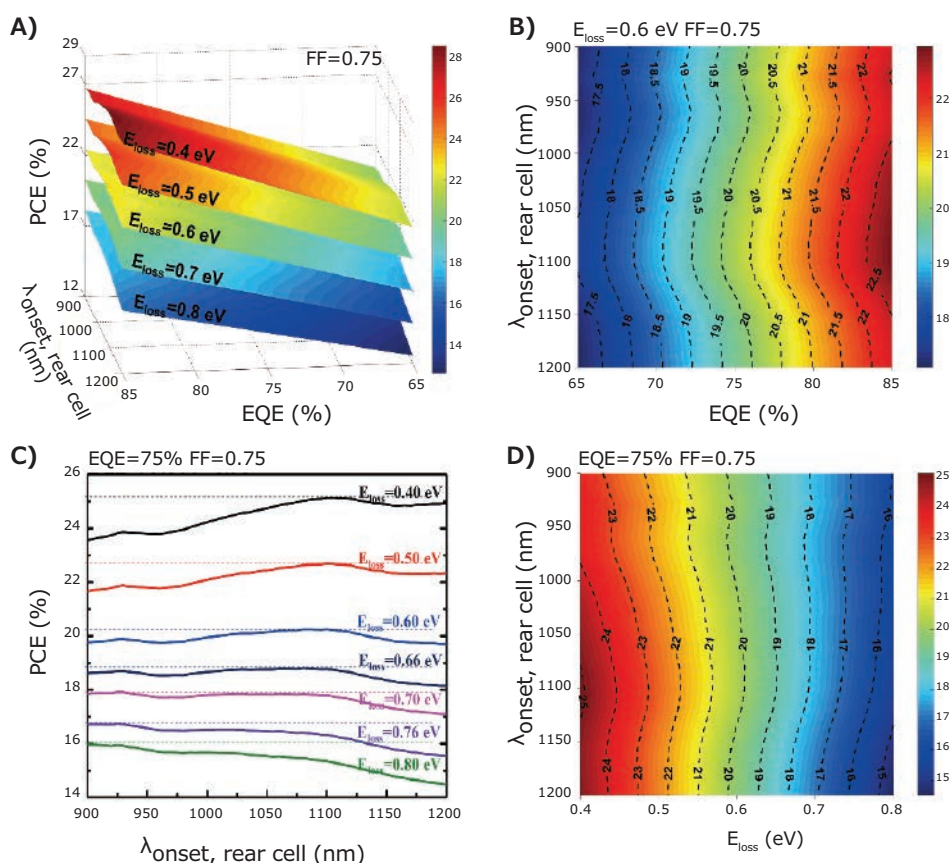


Figure 3. Predicted PCEs of 2T tandem solar cells based on semi-empirical analysis under AM 1.5G. **A)** PCEs versus EQE and $\lambda_{\text{onset, rear cell}}$ with assuming the E_{loss} of each subcell in the range of 0.4–0.8 eV and a fixed FF of 0.75. **B)** PCEs versus EQE and $\lambda_{\text{onset, rear cell}}$ with assumed E_{loss} of 0.6 eV and FF of 0.75. **C)** PCEs versus $\lambda_{\text{onset, rear cell}}$ with E_{loss} of 0.4, 0.5, 0.6, 0.66, 0.7, 0.76 and 0.8 eV, FF of 0.75 and EQE of 75%. **D)** PCEs versus E_{loss} and $\lambda_{\text{onset, rear cell}}$ with assumed EQE of 75% and FF of 0.75. Reproduced with permission from reference 10, copyright 2018 The American Association for the Advancement of Science.

Bu using these rules and the related modelling results, tandem solar cells with PCE of over 17% has been achieved.¹⁰ In the near future, PCEs of over 25% will be achieved provided that researchers can reach an EQE of 80%, E_{loss} of 0.45 eV and FF of 0.75 with a broad absorption onset of ~ 1050 nm using material design and device optimization. The realization of such results would hopefully push the commercialization of the organic photovoltaic technologies forward.

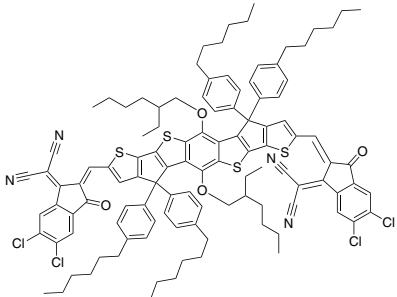
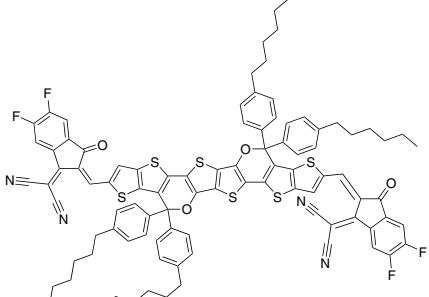
Acknowledgments

The authors gratefully acknowledge the financial support from MoST (2016YFA0200200, 2019YFA0705900), NSFC (51873089, 51773095, 21935007) of China, Tianjin city (17JJCJQC44500, 17JJCZDJC31100) and 111 Project (B12015).

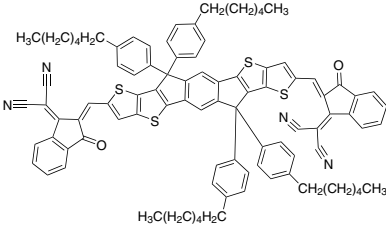
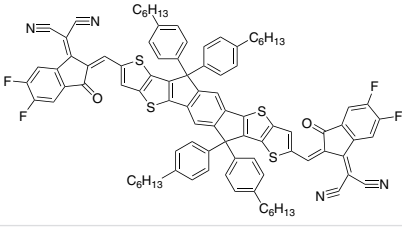
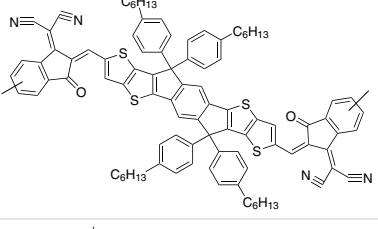
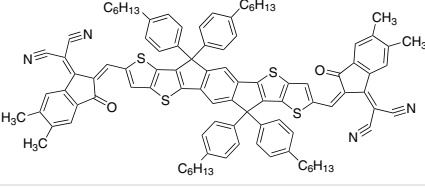
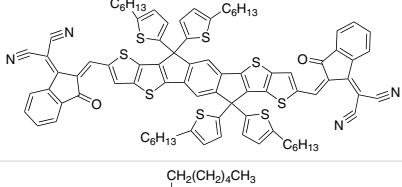
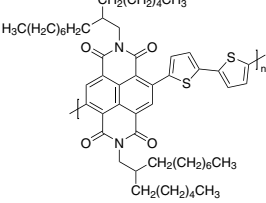
Reference

- Hou, J.; Inganäs, O.; Friend, R. H.; Gao, F. *Nat. Mater.* **2018**, *17*, 119.
- Zhang, G.; Zhao, J.; Chow, P. C. Y.; Jiang, K.; Zhang, J.; Zhu, Z.; Zhang, J.; Huang, F.; Yan, H. *Chem. Rev.* **2018**, *118*, 3447.
- Cheng, P.; Li, G.; Zhan, X.; Yang, Y. *Nat. Photon.* **2018**, *12*, 131.
- Yuan, J.; Zhang, Y.; Zhou, L.; Zhang, G.; Yip, H.-L.; Lau, T.-K.; Lu, X.; Zhu, C.; Peng, H.; Johnson, P. A.; Leclerc, M.; Cao, Y.; Ulanski, J.; Li, Y.; Zou, Y. *Joule* **2019**, *3*, 1140.
- Xu, X.; Feng, K.; Bi, Z.; Ma, W.; Zhang, G.; Peng, Q. *Adv. Mater.* **2019**, *31*, 1901872.
- Fan, B.; Zhang, D.; Li, M.; Zhong, W.; Zeng, Z.; Ying, L.; Huang, F.; Cao, Y. *Sci. China Chem.* **2019**, *62*, 746.
- Ameri, T.; Li, N.; Brabec, C. J. *Energy & Environ. Sci.* **2013**, *6*, 2390.
- Ameri, T.; Dennler, G.; Lungenschmied, C.; Brabec, C. J. *Energy & Environ. Sci.* **2009**, *2*, 347.
- Di Carlo Rasi, D.; Janssen, R. A. J. *Adv. Mater.* **2019**, *31*, 1806499.
- Meng, L.; Zhang, Y.; Wan, X.; Li, C.; Zhang, X.; Wang, Y.; Ke, X.; Xiao, Z.; Ding, L.; Xia, R.; Yip, H.-L.; Cao, Y.; Chen, Y. *Science* **2018**, *361* (6407), 1094.
- Zheng, Z.; Zhang, S.; Zhang, J.; Qin, Y.; Li, W.; Yu, R.; Wei, Z.; Hou, J. *Adv. Mater.* **2016**, *28*, 5133.
- Li, M.; Gao, K.; Wan, X.; Zhang, Q.; Kan, B.; Xia, R.; Liu, F.; Yang, X.; Feng, H.; Ni, W.; Wang, Y.; Peng, J.; Zhang, H.; Liang, Z.; Yip, H.-L.; Peng, X.; Cao, Y.; Chen, Y. *Nat. Photon.* **2016**, *11*, 85.
- Li, G.; Chang, W.-H.; Yang, Y. *Nat. Rev. Mater.* **2017**, *2*, 17043.
- Kan, B.; Feng, H.; Yao, H.; Chang, M.; Wan, X.; Li, C.; Hou, J.; Chen, Y. *Sci. China Chem.* **2018**, *61*, 1307.
- Li, W.; Ye, L.; Li, S.; Yao, H.; Ade, H.; Hou, J. *Adv. Mater.* **2018**, *30*, 1707170.
- Liu, W.; Li, S.; Huang, J.; Yang, S.; Chen, J.; Zuo, L.; Shi, M.; Zhan, X.; Li, C.-Z.; Chen, H. *Adv. Mater.* **2016**, *28*, 9729.
- Chen, S.; Zhang, G.; Liu, J.; Yao, H.; Zhang, J.; Ma, T.; Li, Z.; Yan, H. *Adv. Mater.* **2017**, *29*, 1604231.
- Shi, X. L.; Zuo, L. J.; Jo, S. B.; Gao, K.; Lin, F.; Liu, F.; Jen, A. K. Y. *Chem. Mater.* **2017**, *29*, 8369.
- Cui, Y.; Yao, H.; Gao, B.; Qin, Y.; Zhang, S.; Yang, B.; He, C.; Xu, B.; Hou, J. *J. Am. Chem. Soc.* **2017**, *139*, 7302.
- Cui, Y.; Yao, H.; Yang, C.; Zhang, S.; Hou, J. *Acta Polym. Sin.* **2018**, *2*, 223.
- Che, X.; Li, Y.; Qu, Y.; Forrest, S. R. *Nat. Energy* **2018**, *3*, 422.
- Cheng, P.; Liu, Y.; Chang, S.-Y.; Li, T.; Sun, P.; Wang, R.; Cheng, H.-W.; Huang, T.; Meng, L.; Nurreyeva, S.; Zhu, C.; Wei, K.-H.; Sun, B.; Zhan, X.; Yang, Y. *Joule* **2019**, *3*, 432-442.
- Liu, G.; Jia, J.; Zhang, K.; Jia, X. e.; Yin, Q.; Zhong, W.; Li, L.; Huang, F.; Cao, Y. *Adv. Energy Mater.* **2019**, *9*, 1803657.
- Zhang, Y.; Kan, B.; Sun, Y.; Wang, Y.; Xia, R.; Ke, X.; Yi, Y. Q.; Li, C.; Yip, H. L.; Wan, X.; Cao, Y.; Chen, Y. *Adv. Mater.* **2018**, *30*, 1707508.
- Meng, L.; Yi, Y. Q.; Wan, X.; Zhang, Y.; Ke, X.; Kan, B.; Wang, Y.; Xia, R.; Yip, H. L.; Li, C.; Chen, Y. *Adv. Mater.* **2019**, *31*, 1804723.

Non-Fullerene Acceptors

Name	Structure	Purity/Molecular Weight	Cat. No.
BT-CIC		$\geq 98\%$	906824-100MG
COi8DFIC		$\geq 98\%$	906379-100MG

Name	Structure	Purity/Molecular Weight	Cat. No.
Copper(II)		-	446653-1G
Di-PDI		≥97%	900774-100MG
EH-IDTBR		97%	900853-50MG 900853-100MG
FBR		≥97%	900854-50MG 900854-100MG
F-M		≥98%	906972-100MG
Hexyl N-annulated perylene diimide		-	901144-500MG
IDT-2Br		≥99% 1518.20 g/mol	910635-100MG
O-IDTBR		99%	900810-50MG 900810-100MG

Name	Structure	Purity/Molecular Weight	Cat. No.
ITIC		99%	900799-50MG 900799-100MG
ITIC-F		97%	901423-100MG
ITIC-M		≥97%	900947-50MG 900947-100MG
ITIC-Cl		98%	906387-100MG
ITIC-DM		99%	900803-50MG 900803-100MG
ITIC-Th		99%	900800-50MG 900800-100MG
N2300		average M_n 25-50 kDa	900962-100MG 900962-500MG

Name	Structure	Purity/Molecular Weight	Cat. No.
P(NDI2OD-T2)		average M_n 50-100 kDa	900961-100MG 900961-500MG
PDI-DPP-PDI		-	901143-100MG
Perylene-3,4,9,10-tetracarboxylic dianhydride		97%	P11255-25G P11255-100G
Poly(benzimidazobenzophenanthroline)		-	667846-250MG 667846-1G
SF-PDI		99%	900782-100MG
TPDI-Hex		-	901146-250MG
Y6		≥99%	908509-100MG

Polymeric Donors

Wide-Bandgap Polymeric Donors

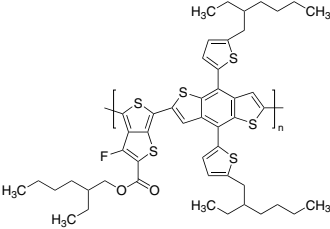
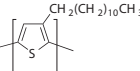
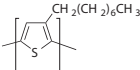
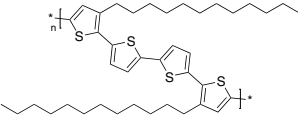
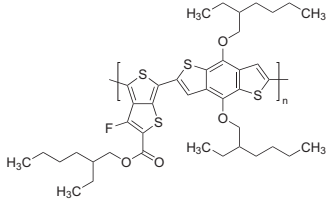
Name	Structure	Molecular Weight	Cat. No.
J51		M_w 40,000-80,000 by GPC (PS standard)	901058-100MG
J61		M_w 50,000-100,000 by GPC (PS standard)	901045-100MG
PBDB-T		M_w >50,000 by GPC (GPC standard: PS)	901099-100MG
PBDB-T-2Cl		50,000-100,000 g/mol by GPC	906352-100MG
PBDB-T-2F		M_w 80,000-200,000 g/mol by GPC	906336-100MG
PBDB-T-SF		M_w ≥80,000	906344-100MG

Name	Structure	Molecular Weight	Cat. No.
PBDTS-TDZ		average $M_n > 30000$ average $M_w > 60000$	901871-100MG
PBDT-TPD		average M_n 10,000-50,000	776300-100MG
PBDTTT-C-T		M_w 80,000-150,000 (GPC, PS standard)	901067-100MG
PBTTPD		average M_n 3,500-20,000 g/mol	745901-100MG
PCDTBT		average M_w 100,000-140,000	753998-100MG
PDBT-T1		M_w 20,000-50,000 (GPC, PS standard)	901097-100MG
PFO-DBT		average M_w 10,000-50,000	754013-100MG

Name	Structure	Molecular Weight	Cat. No.
Poly[2-methoxy-5-(2-ethylhexyloxy)-1,4-phenylenevinylene]	<p>R = </p>	average M_n 40,000-70,000	541443-250MG 541443-1G
	<p>R = </p>	-	536512-1G
TQ1		average M_n 12,000-45,000 g/mol	745898-100MG

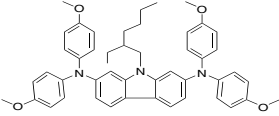
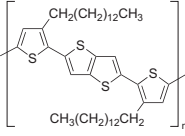
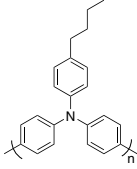
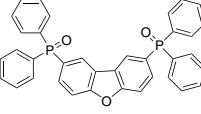
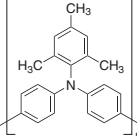
Medium- and Low-Bandgap Polymeric Donors

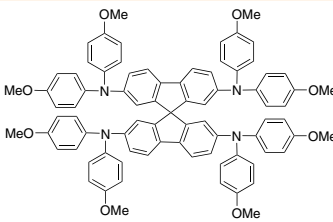
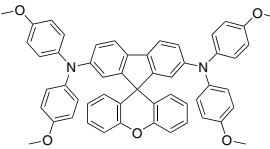
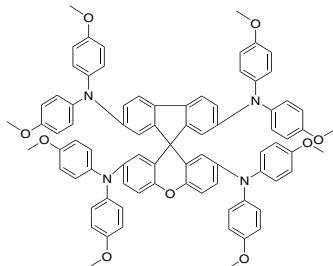
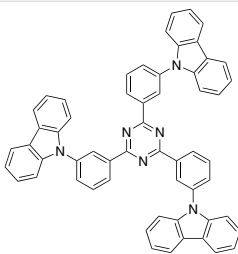
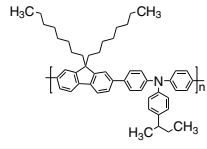
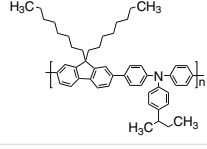
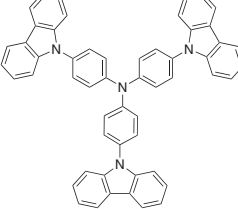
Name	Structure	Molecular Weight	Cat. No.
MDMO-PPV		$M_n \sim 120,000$	546461-250MG 546461-1G
MEH-PPV average M_n 70,000-100,000 MEH-PPV	<p>R = </p>	average M_n 70,000-100,000	541435-1G
PBDTTT-CF		average M_w 53,000-83,000 by GPC	772402-100MG
PCPDTBT		average M_w 7,000-20,000	754005-100MG
PDTSTPD		average M_n 7,000-35,000 by GPC	745928-100MG
PffBT4T-2OD		M_w 100,000-150,000 by GPC	900720-100MG
PffBT4T-C9C13		M_w 35,000-100,000	900980-100MG

Name	Structure	Molecular Weight	Cat. No.
Poly([2,6'-4,8-di(5-ethylhexylthienyl)benzo[1,2-b;3,3-b]dithiophene]{3-fluoro-2[(2-ethylhexyl)carbonyl]thieno[3,4-b]thiophenediyl})		>145,000	794333-100MG
Poly(3-dodecylthiophene-2,5-diyl)		average $M_w \sim 27,000$	682780-250MG
Poly(3-octylthiophene-2,5-diyl)		average $M_n \sim 25,000$	682799-250MG
PQT-12		-	906921-500MG
PTB7		average M_w 80,000-200,000	772410-100MG

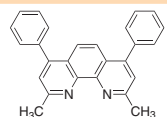
Interfacial Materials

Hole-Transport Materials

Name	Structure	Purity/Molecular Weight	Cat. No.
EH44		$\geq 99\%$, HPLC	906395-1G
PBTTT-C14		$M_w > 50,000$	753971-250MG
Poly-TPD		>20,000 g/mol	907065-1G
PPF		97%	901342-250MG
PTAA		average M_n 7,000-10,000 (GPC)	702471-100MG 702471-1G

Name	Structure	Purity/Molecular Weight	Cat. No.
SHT-263 Solarpur®		>99%	902500-1G 902500-10G
Spiro[9H-fluorene-9,9'-(9H)xanthene]-2,7-diamine		≥98%	904899-1G
Spiro[9H-fluorene-9,9'-(9H)xanthene]-2,2',7,7'-tetramine		>98%	906018-1G
TCPZ		-	900969-500MG
TFB		-	L512036-250MG
TFB		average M_w >30,000 by GPC	901101-250MG 901101-1G
Tris(4-carbazoyl-9-ylphenyl)amine		97%	688053-1G 688053-5G

Other Buffer Layer Materials

Name	Structure	Purity/Molecular Weight	Cat. No.
Bathocuproine		96%	140910-500MG 140910-1G

Name	Structure	Purity/Molecular Weight	Cat. No.
Bathocuproine		99.99% trace metals basis	699152-500MG 699152-5G
Molybdenum(VI) oxide	MoO ₃	99.97% trace metals basis	203815-5G 203815-25G
Nickel(II) oxide	NiO	≥99.995% trace metals basis	481793-5G 481793-25G
Nickel(II) oxide	NiO	99.99% trace metals basis	203882-20G 203882-100G
Nickel(II) oxide	NiO	-	774545-500MG
PFN-Br		M _w 30,000-50,000 by GPC	906980-100MG
Poly(3,4-ethylenedioxythiophene)-poly(styrenesulfonate)		-	655201-5G 655201-25G
Poly(3,4-ethylenedioxythiophene)-poly(styrenesulfonate)	-	-	900181-100G
Polypyrrole		-	577030-5G 577030-25G
Polypyrrole		-	530573-25G
Polypyrrole-block-poly(caprolactone)		-	735817-25G
Vanadium(V) oxide	V ₂ O ₅	99.95% trace metals basis	204854-1G 204854-5G 204854-25G
Vanadium(V) oxide	V ₂ O ₅	≥99.6% trace metals basis	221899-5G 221899-250G 221899-1KG
Vanadium(V) oxide	V ₂ O ₅	≥98%	223794-100G 223794-500G

Building Blocks

Name	Structure	Purity	Cat. No.
2,1,3-Benzothiadiazole-4,7-bis(boronic acid pinacol ester)		95%	702803-1G
2,5-Bis(trimethylstannyl)thiophene		97%	738891-1G 738891-5G
2,5-Dibromo-3,4-dihexylthiophene		97%	752541-1G 752541-5G
3,4-Dihydroxy-3-cyclobutene-1,2-dione		99%	123447-5G 123447-25G 123447-100G

Name	Structure	Purity	Cat. No.
4,4'-Dimethoxydiphenylamine		99%	767905-1G 767905-5G
9,9-Dioctylfluorene-2,7-diboronic acid bis(1,3-propanediol) ester		97%	569356-1G 569356-5G
2-Ethylhexyl 4,6-dibromo-3-fluorothiopheno[3,4-b]thiophene-2-carboxylate		≥97%	901228-250MG
1,3,5-Tris(bromomethyl)benzene		97%	657336-5G 657336-10G

High Purity Electronic Grade Electrolytes

Name	Structure	Purity	Cat. No.
1-Butyl-3-methylimidazolium bis(trifluoromethylsulfonyl)imide Solarpur®		≥99.5%, HPLC	901041-25G
1-Propyl-3-methyl-imidazolium bis(trifluoromethylsulfonyl)imide Solarpur®		≥99.0%, HPLC	901024-25G

Substrates and Electrode Materials

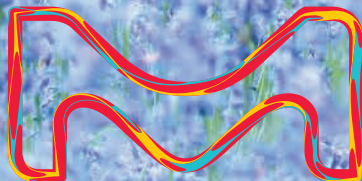
Name	Surface Resistivity (Ω/sq)	L × W × Thickness (mm)	Cat. No.
Fluorine doped tin oxide coated glass slide	~7	50 × 50 × 2.2	735140-5EA
	~7	100 × 100 × 2.3	735159-5EA
	~7	300 × 300 × 2.2	735167-1EA
	~8	50 × 50 × 3	735175-5EA
	~8	100 × 100 × 3	735183-5EA
	~8	300 × 300 × 3.2	735191-1EA
Indium oxide coated PET	≤10	150 × 150 × 0.2	700177-5PAK 700177-10PAK
	5-15	75 × 25 × 1.1	576360-10PAK 576360-25PAK
Indium tin oxide coated glass slide, rectangular	8-12	75 × 25 × 1.1	578274-10PAK 578274-25PAK
	15-25	75 × 25 × 1.1	636916-10PAK 636916-25PAK
Indium tin oxide coated glass slide, square	8-12	25 × 25 × 1.1	703192-10PAK
	30-60	25 × 25 × 1.1	703184-10PAK
Indium tin oxide coated PET	60	1 ft × 1 ft × 5 mil	639303-1EA 639303-5EA
	100	1 ft × 1 ft × 5 mil	639281-1EA 639281-5EA
	60	1 ft × 1 ft × 7 mil	749729-1EA 749729-5EA
	100	1 ft × 1 ft × 7 mil	749737-1EA 749737-5EA

SEE THE FUTURE OF solvents

Why choose between solvents that are ecological and those that are reliable? Enjoy both with high-quality, environmentally friendly alternatives. Our growing portfolio includes **BioRenewable solvents** from waste feedstock that avoid using non-renewable resources, as well as **greener alternative solvents** to replace those posing health or environmental risks. A perfect example is our award-winning Cyrene™ solvent – a safer, bio-based alternative to DMF and NMP – made from renewable cellulose waste in an almost energy-neutral process that releases water.

We're dedicated to supporting all your explorations responsibly. See how easy it is to switch to sustainable lab practices on:

SigmaAldrich.com/biorenewable



The life science
business of Merck
KGaA, Darmstadt,
Germany operates as
MilliporeSigma in the
U.S. and Canada.

Sigma-Aldrich®
Lab & Production Materials

MilliporeSigma
400 Summit Drive
Burlington, MA 01803

sciencesational chemistry

MILLIPORE
SIGMA

empowering your discovery

Scientific discovery demands creativity, competence, and courage. You have what it takes. We support you with everything else.

Don't let anything get in the way of your next breakthrough. Whether you are pushing the boundaries of organic synthesis, materials science, or life science, we give you fast access to cutting-edge chemistry. We boost your innovation through a vast database of chemicals, protocols and publications. And we help fast-track breakthroughs through partnerships with the brightest minds in chemistry. Experience bolder chemistry for greater discovery.

Discover how we help you to stay sciencesational on:
SigmaAldrich.com/sciencesational



© 2020 Merck KGaA, Darmstadt, Germany and/or its affiliates. All Rights Reserved. MilliporeSigma, the vibrant M, and Sigma-Aldrich are trademarks of Merck KGaA, Darmstadt, Germany or its affiliates. All other trademarks are the property of their respective owners. Detailed information on trademarks is available via publicly accessible resources.
Lit. No. MS_BR5351EN
2020 - 30343 04/2020

The life science business of Merck KGaA, Darmstadt, Germany operates as MilliporeSigma in the U.S. and Canada.

Sigma-Aldrich®
Lab & Production Materials